HIGH OPERATING TEMPERATURE MID-WAVE INFRARED HgCdTe PHOTODIODE DESIGN

A THESIS SUBMITTED TO
THE GRADUATE SCHOOL OF NATURAL AND APPLIED SCIENCES
OF
MIDDLE EAST TECHNICAL UNIVERSITY

BY

ERAY YURTSEVEN

IN PARTIAL FULFILLMENT OF THE REQUIREMENTS
FOR
THE DEGREE OF MASTER OF SCIENCE
IN
ELECTRICAL AND ELECTRONICS ENGINEERING

SEPTEMBER 2019

Approval of the thesis:

HIGH OPERATING TEMPERATURE MID-WAVE INFRARED HGCDTE PHOTODIODE DESIGN

submitted by **ERAY YURTSEVEN** in partial fulfillment of the requirements for the degree of **Master of Science in Electrical and Electronics Engineering Department, Middle East Technical University** by,

Prof. Dr. Halil Kalıpçılar
Dean, Graduate School of **Natural and Applied Sciences** _____

Prof. Dr. İlkay Ulusoy
Head of Department, **Electrical and Electronics Eng.** _____

Assist. Prof. Dr. Serdar Kocaman
Supervisor, **Electrical and Electronics Eng., METU** _____

Examining Committee Members:

Prof. Dr. Cengiz Beşikçi
Electrical and Electronics Eng., METU _____

Assist. Prof. Dr. Serdar Kocaman
Electrical and Electronics Eng., METU _____

Prof. Dr. Raşit Turan
Physics, METU _____

Assoc. Prof. Dr. Mustafa Kulakçı
Physics, Eskişehir Technical University _____

Assist. Prof. Dr. Selçuk Yerci
Electrical and Electronics Eng., METU _____

Date: 06.09.2019

I hereby declare that all information in this document has been obtained and presented in accordance with academic rules and ethical conduct. I also declare that, as required by these rules and conduct, I have fully cited and referenced all material and results that are not original to this work.

Name, Surname: Eray Yurtseven

Signature:

ABSTRACT

HIGH OPERATING TEMPERATURE MID-WAVE INFRARED HGCDTE PHOTODIODE DESIGN

Yurtseven, Eray
Master of Science, Electrical and Electronics Engineering
Supervisor: Assist. Prof. Dr. Serdar Kocaman

September 2019, 81 pages

Infrared focal plane arrays are critical components in many of the military and civilian applications for advanced imaging systems. HgCdTe is one of the most widely used infrared detector material. An important issue with this material for thermal imaging system is the operating temperature as it determines cryocooler crucial characteristics, namely power comsumption and device lifetime. Therefore, there is an effort towards to operate at higher temperatures, but performance characteristics need to be carefully designed. Increasing operating temperature causes to increase diode current due to thermal generation and also is associated with 1/f noise. Furthermore, number of defective diodes increases at high operating temperatures. High quality material is the first requirement to maintain the same diode characteristic at higher temperatures. This can be achieved by using Molecular Beam Epitaxy (MBE) method that provides ultra-high vacuum condition and ultra-pure materials (Hg, CdTe, Te). Further way to improve diode characteristics at higher temperatures is applying design modifications. For instance, adjusting absorber layer parameters such as thickness, cadmium mole fraction and doping level or adding some extra layers to diode structure. Barrier detectors, auger suppression structures and photon trapping structures are the major high operating temperature (HOT) infrared detector configurations. Within the scope of this thesis, a new HgCdTe MWIR photodiode is designed by interpreting HOT

structures which are mentioned above. With the designed structure, it was observed that the dark current improved at all temperatures between 100 K and 300 K. The quantum efficiency decreased by 3.1% at -0.1 V due to barrier layer in the designed structure. However, this reduction was reduced to 1.2% by photon trapping structure. This structure also provided an improvement of about 18.2% in the dark current. This improvement is consistent with volume reduction in the photodiode. The surface component of the dark current was not included in the simulations. Therefore, during the fabrication of the designed structure, passivation of the mesa walls need to be done well to prevent large surface leakage current.

Keywords: High operating temperature, HgCdTe, MWIR, infrared radiation

ÖZ

YÜKSEK ÇALIŞMA SICAKLIĞINDA ORTA DALGABOYU KIZILÖTESİ HgCdTe FOTODİYOT TASARIMI

Yurtseven, Eray
Yüksek Lisans, Elektrik ve Elektronik Mühendisliği
Tez Danışmanı: Dr. Öğr. Üyesi Serdar Kocaman

Eylül 2019, 81 sayfa

Kızılötesi odak düzlem dizinleri ileri seviye görüntüleme sistemleri için en kritik bileşendir. Birçok askeri ve sivil uygulamalarda kullanılırlar. HgCdTe en çok kullanılan kızılötesi algılayıcı malzemelerinden biridir. Termal görüntüleme sistemi için bu malzemeyle ilgili önemli bir konu, güç tüketimi ve cihazın kullanım ömrü ile, suğutma donanımının önemli özelliklerini belirlediği için çalışma sıcaklığıdır. Bu nedenle, daha yüksek sıcaklıklarda çalışmaya yönelik bir çaba vardır, ancak performans özelliklerinin dikkatlice tasarlanması gerekir. Çalışma sıcaklığının arttırılması, termal jenerasyon nedeniyle diyot akımını arttırır ve bu durum 1 / f gürültü ile de ilişkilidir. Ayrıca, hatalı diyotların sayısı artar ve çalışma sıcaklığı artar. Yüksek kaliteli malzeme, aynı diyot karakteristiğini yüksek sıcaklıklarda korumak için ilk şarttır. MBE yöntemiyle bu başarılabilir. Bu yöntem yüksek vakum durumu ve yüksek saflıkta malzeme (Hg, CdTe, Te) kullanım imkanı sağlıyor. Diyot özelliklerini daha yüksek sıcaklıklarda iyileştirmenin diğer bir yolu da tasarım değişiklikleri uygulamaktır. Örneğin, kalınlık, kadmiyum mol fraksiyonu ve doping seviyesi gibi emici tabaka parametrelerinin ayarlanması veya diyot yapısına fazladan bazı katmanlar eklenmesi. Bariyer dedektörleri, burgu bastırma yapıları ve foton yakalama yapıları önemli yüksek çalışma sıcaklığı (YÇS) kızılötesi dedektör konfigürasyonlardır. Bu tez kapsamında yukarıda belirtilen YÇS yapılar

yorumlanarak yeni bir HgCdTe MWIR fotodiyot tasarlandı. Tasarlanan yapıyla, karanlık akımın 100 K ve 300 K arasındaki tüm sıcaklıklarda geliştiği görülmüştür. Kuantum verimi, tasarlanmış yapıdaki bariyer tabakası nedeniyle -0,1 V'da % 3,1 oranında azalmıştır. Ancak, bu azalma, foton yakalama yapısı ile % 1,2'ye düşürüldü. Bu yapı aynı zamanda karanlık akımda yaklaşık % 18,2'lik bir iyileşme sağlamıştır. Bu gelişme, fotodiyottaki hacim azalması ile tutarlıdır. Simülasyonlara karanlık akımın yüzey bileşeni dahil edilmedi. Bu nedenle, tasarlanan yapının imalatı sırasında, büyük yüzey kaçağı akımını önlemek için mesa duvarlarının pasifleştirilmesi iyi yapılmalıdır.

Anahtar Kelimeler: Yüksek çalışma sıcaklığı, HgCdTe, MWIR, kızılötesi radyasyon

To my family

ACKNOWLEDGEMENTS

I would like to thank to my thesis advisor Asst. Prof. Dr. Serdar Kocaman for his excellent guidance and supervision. It would not be possible to complete this study without his continuous support and motivation.

I also want to thank Prof. Dr. Cengiz Beşikçi for giving me the chance to work in a well-equipped facility and sharing his immense knowledge.

I would like to thank Prof. Dr. Raşit Turan, Assoc. Prof. Dr. Mustafa Kulakçı, and Assist. Prof. Dr. Selçuk Yerci for being in my thesis committee.

I would like to give special thanks to Mr. Kaan Sel, Mr. Yiğit Özer and Mr. Utku Karaca for their invaluable friends and sharing knowledge with me.

Last but the best, I want to express my deep love and gratitude to my wife Öznur and my daughter Ada for being always with me.

TABLE OF CONTENTS

LIST OF TABLES

TABLES

LIST OF FIGURES

FIGURES

LIST OF ABBREVIATIONS

IR	Infrared
MWIR	Mid Wave Infrared
HOT	High Operating Temperature
HgCdTe (MCT)	Mercury Cadmium Telluride
GaAs	Gallium Arsenide
Si	Silicon
FPA	Focal Plane Array
SWIR	Short Wave Infrared
LWIR	Long Wave Infrared
VLWIR	Very Long Wave Infrared
QE	Quantum Efficiency
SNR	Signal to Noise Ratio
G-R	Generation-Recombination
SRH	Schockley-Read-Hall
BLIP	Background Limited Performance
CZT	Cadmium Zinc Telluride
MBE	Molecular Beam Epitaxy
BBT	Band to Band Tunneling
TAT	Trap Assisted Tunneling

LIST OF SYMBOLS

T	Temperature
h	Planck's constant
c	The speed of light in vacuum
k	Boltzmann constant
q	Electric charge
λ	Wavelength
λ_c	Cut off wavelength
E_g	Bandgap energy
η	Quantum efficiency
Φ	The incident photon flux density
f	Frequency
D_n	Diffusion constant for electrons
D_p	Diffusion constant for holes
L_n	Diffusion length for electrons
L_p	Diffusion length for holes
μ_n	Electron mobility
μ_p	Hole mobility
τ_n	Electron lifetime
τ_p	Hole lifetime
n	Free carrier electron concentration

p	Free carrier hole concentration
W	Width of depletion region
E_F	Fermi level for a semiconductor
E_i	Intrinsic energy level for a semiconductor
E_t	Trap energy level for a semiconductor
E_c	Conduction band level for a semiconductor
E_v	Valance band level for a semiconductor
N_d	Donor concentration
N_a	Acceptor concentration
E	Electric field
m_e	Electron mass
m_h	Hole mass
c_n	Capture coefficient of electrons
c_p	Capture coefficient of holes
m_e^*	Effective mass of electrons
m_h^*	Effective mass holes
N_c	Effective density of states in the conduction band
N_v	Effective density of states in the valance band
ε	Dielectric constant
i_n	Noise current spectral density

CHAPTER 1

INTRODUCTION

1.1. Infrared Radiation

In this section, the definition of infrared radiation and the general information about different spectral bands will be explained.

1.1.1. The Electromagnetic Spectrum

Any electromagnetic radiation can be broken down into a set of monochromatic waves. Each monochromatic wave is characterized by its amplitude and its wavelength. The electromagnetic spectrum corresponds to the classification of electromagnetic radiation by frequency or wavelength, and extends from the zero frequency to the infinite frequency, as shown in Figure 1.1 [1]. The infrared domain is between the visible and the microwaves.

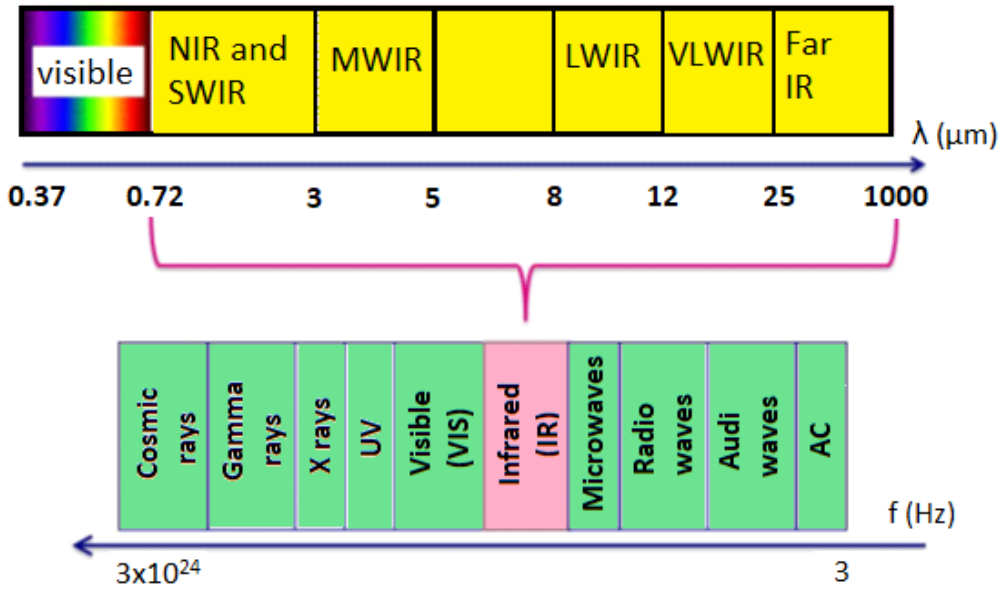

Figure 1.1: Electromagnetic spectrum (redrawn as in the ref [1])

Infrared detection is based on the fact that all bodies radiate in a given spectral range, related to their temperature. Indeed, all bodies whose temperature is greater than absolute zero emit infrared radiation. Thus, the presence of a light source (sun, star, moon ...) is not essential for the IR detection of these naturally luminous bodies. This type of imaging is called "passive" since no external stimulus intervenes in the emission of radiation.

1.1.2. Atmospheric Transmission

As shown in Figure 1.2 [2], we mainly define four spectral bands in IR that are:

- (SWIR) Short Wavelength Infrared between 0.78 µm and 3 µm
- (MWIR) Mid-wavelength Infrared between 3 µm and 5 µm
- (LWIR) Long Wavelength Infrared between 8 µm and 12 µm
- (VLWIR) Very Long Wavelength Infrared between 12 µm and 20 µm

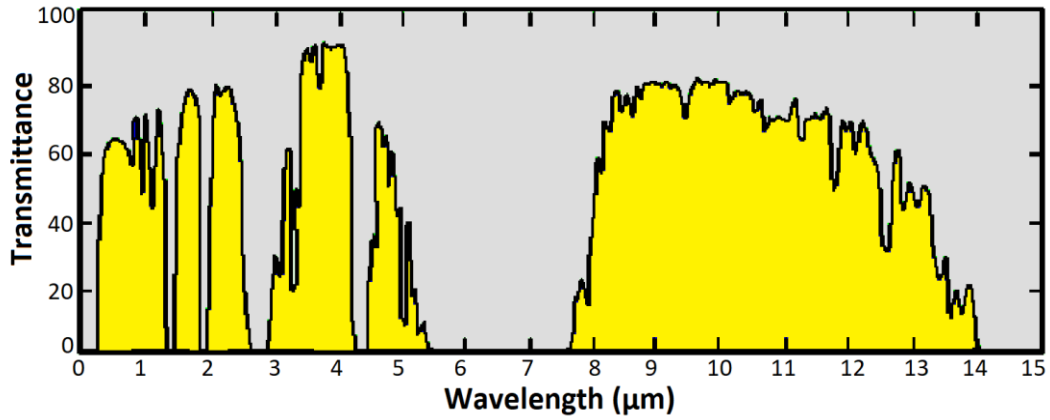

Figure 1.2: Atmospheric transmission spectrum of the light (redrawn as in the ref [2])

These bands are related to the windows of transparency of the atmosphere, and their definition can change according to the field of application.

1.2. Types of Infrared Detectors

There are two main lines of IR detectors: photon detectors and thermal detectors [2]. Their characteristics will be presented in the following paragraphs.

1.2.1. Thermal Detectors

Thermal sensors are sensitive to the temperature rise of an incident IR absorber. To do this, they use the thermal agitation of the electrons caused by the incident photons. The incident IR radiation causes a temperature difference of the absorber, which affects some of its physical properties, thus causing a modification of the measured electrical signal. The physical properties concerned are: a potential difference for thermopiles, resistivity for bolometers, and spontaneous internal polarization for pyro electric detectors. A general property of all these thermal detectors is the fact that only the total energy of the photons is counted, so there is no spectral signature specific to the detector.

The microbolometer is an example where the elementary detector consists of a very thin membrane suspended by nails to provide thermal insulation concerning the rest of the component [3]. It plays the role of the absorber whose temperature variations are measured through a change of resistivity to evaluate the incident IR radiation.

Thermal detectors operate at room temperature. This greatly reduces their cost, and makes them easier to use. As opposed to the photon detectors, which must be cooled, the thermal detectors are also called "uncooled detectors". However, they are less sensitive than photon detectors, with larger time constants.

As a result of this cost reduction, these detectors are increasingly present in the civil sphere. Among the many applications are thermography, monitoring, and driving assistance systems [3].

1.2.2. Photon Detectors

Photon detectors use the photoelectric effect to measure the incident photon flux, which generates a current resulting from the excitation process. There are several technological fields of photon detectors, which can be classified into two categories:

- Photovoltaic detectors, in which the detection structure is based on a p-n junction. Various architectures exist, such as solid bulk semiconductor detectors.

- Photoconductors, which are based on the use of an n type or a p type semiconductor. A voltage need to be applied for detection of incident photons. Well known architectures include the bulk materials and the multi-quantum wells.

In contrast to thermal detectors, these detectors need to be cooled for MWIR and LWIR region so that the thermal agitation of the electrons usually does not disturb the measured signal. They are also called "cooled detectors". These detectors have a very characteristic spectral signature.

1.3. Characteristics of Photovoltaic Detectors

In this section, the basic features of photon detectors will be presented. First of all the principle of photons detection will be explained. Next, semiconductor doping and PN junction structure will be explained. Lastly, the advantages and disadvantages of photon detectors will be specified.

1.3.1. Detection Principle in a Semiconductor Material

A photon detector uses a semiconductor material that generates electron/hole pairs from incoming photons. The crystallographic structure of the semiconductor material determines the spectral range of application. More precisely, the energy bandgap depends on its lattice constant, as well as on the nature of the atoms of the elementary crystal lattice, as shown in Figure 1.3 [4].

It may be noted in particular that the HgCdTe material, which we focus on in this work, covers all spectral ranges of IR detection, since this ternary alloy is composed of a semi-metal (HgTe) and a wide bandgap semiconductor (CdTe) (Figure 1.3).

Detection in a semiconductor is based on the band theory, according to which an electron within a periodic atomic structure can take only discrete and quantized energy values. Photon detectors are also called as “quantum detectors” [5]. The quantum term

comes from the fact that the detection is related to the discretization of these energy levels.

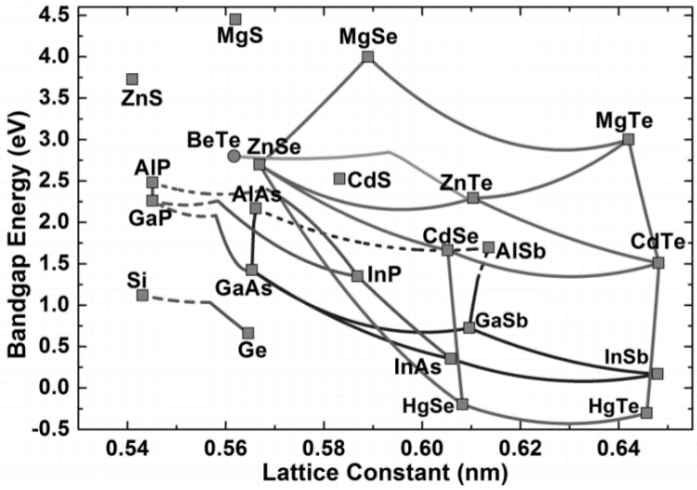

Figure 1.3: Energy bandgap vs lattice constant of some semiconductors (redrawn as in the ref [4])

The crystallographic architecture of a semiconductor contains a multitude of atoms that generate discrete levels of energy allowed for the electrons. These levels are very close to each other, forming a continuum of energy, so-called energy bands. The highest energy band, which is filled fully (at 0K), is called the valence band. The next energy band is called the conduction band, which may contain electrons. The energy gap between these two bands is the bandgap of the semiconductor (see Figure 1.4) [6].

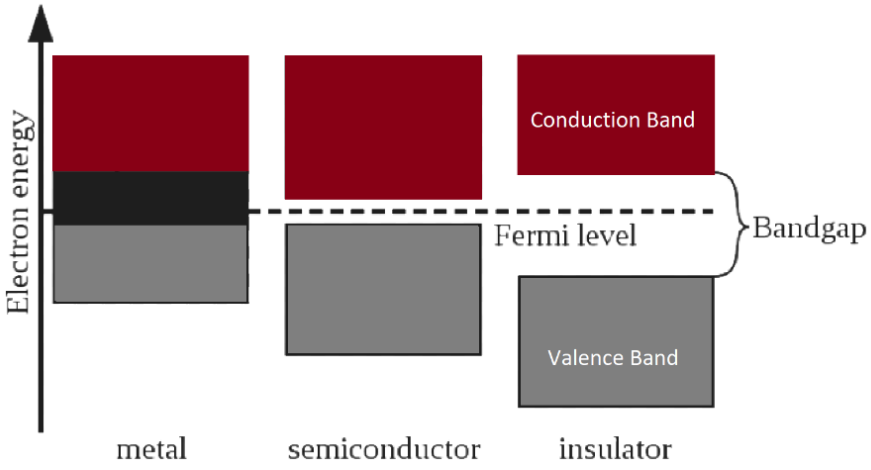

Figure 1.4: Energy band structure of solids (redrawn as in the ref [6])

As shown in Figure 1.4, a semiconductor is actually an intermediate between an insulator, where the gap is too large to create free charge carriers in the conduction band, and a metal, which can be considered as a material with a zero gap allowing all the carriers of charges to be free to circulate in the structure.

The detection process in a semiconductor is based on a generation of electron/hole pair caused by the incident photon, commonly called the photoelectric effect. The photon is absorbed if it has an energy greater than or equal to the semiconductor bandgap. It brings enough energy to excite the electron to higher energy level. The electron goes to the conduction band from the valence band. This creates an electron-hole pair. These electron-hole pairs are electric charge carriers that are free to move in the material. Metal contacts collect them to form the electrical signal.

1.3.2. Semiconductor Doping

Semiconductor doping consists of introducing impurities into the material to create local excess carriers. This consists of a controlled implantation of specific ions in the semiconductor to form the n and p zones. This step is necessary for the control of the electrical conductivity of the semiconductor material.

The n-type material can be obtained by doping the semiconductor with atoms called donors, which are capable of creating excess electrons. In this case, the density of donors is greater than the density of acceptors. The holes are the minority carriers, and the electrons are the majority carriers [7].

In the same way, the p-type material can be obtained by doping the semiconductor with atoms called acceptors, capable of collecting electrons. In these materials, the majority carriers are then the holes, and the electrons are the minority carriers [7].

1.3.3. PN Junction

The principle of photon detection is based on the operation of a p – n junction in photovoltaic detectors. P-N junction consists of the juxtaposition of a zone n and a zone p. When the junction is formed of the same semiconductor material, it is called

homojunction. When it is formed by two different materials (structurally compatible crystal lattices), it is called heterojunction.

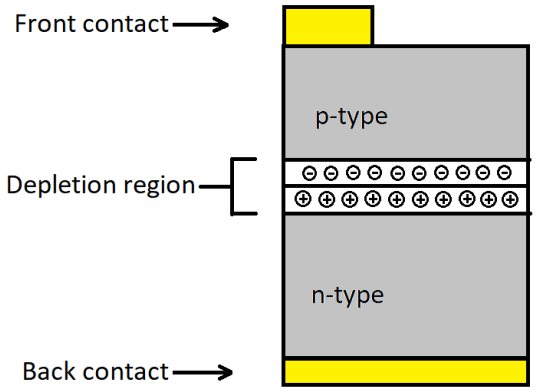

Figure 1.5: Schematic of a typical p-n Junction (redrawn as in the ref [5])

The free carriers cause a diffusion phenomenon. In this process, the majority carriers of each side goes to the other side to recombine. The displacement of the free carriers forms the diffusion current. At the boundary of the two zones, the donor and acceptor atoms form an electric field which opposes the diffusion of the majority carriers, and which maintains the separation of the two types of carriers until reaching the thermodynamic equilibrium [8]. This zone of strong electric field is called the space charge zone.

When a reverse bias applied to the p-n junction, the incident photon flux creates an excess electron-hole pairs with respect to the equilibrium. If these carriers are created in the space charge zone, then they will be immediately separated by the strong electric field. They will migrate each from their side, and be propelled by the electric field towards the zone where they will be in the majority (the holes towards the p side and electrons towards the n side). Finally, the holes or electrons will be collected through an ohmic contact.

If optically generated excess carriers are created outside the space charge zone, and if they are at a distance inferior to their diffusion length, then they may move to the space charge zone, where they will be separated and collected in the same way.

The collection of optically generated carriers with the ohmic contacts will be at the origin of a current called photocurrent that can be measured to evaluate the incident IR flux.

In some cases, created excess carriers may not be collected. For example, suppose that the created carriers are outside the depletion region, and they are at a distance greater than their diffusion length. In this case, the probability of recombination (the electron fills a hole) becomes strong, thereby removing the photogenerated electron-hole pair. Recombination on crystalline defects is the other limitation of the collection of photo-generated carriers.

1.3.4. Advantages of Photon Detectors

The maturity of certain semiconductor materials and varied architectures have led to a considerable improvement in the detector performance. In fact, photon detectors have the advantage of having an excellent response speed and a very high sensitivity.

Moreover, photon detectors imposes a selective detection of photons as a function of their energy, which must be greater than the energy bandgap of the semiconductor, and therefore a function of their wavelength.

All these advantages enable photon detectors to be preferred to thermal detectors, for high performance applications (radiometry, high resolution).

1.3.5. Disadvantages of Photon Detectors

The process of converting photons into electrons can present several possible limits. In fact, the impurities of the semiconductor material used can introduce energy levels close to the valence band and the conduction band, causing the detection of photons of energy that is slightly less than the bandgap. Recombinations of the optically generated electron-hole pairs due to crystalline defects and insufficient diffusion length are also a problem.

Besides, it is necessary to cool photon detectors for thermal detection, to prevent the dark current from being preponderant for the photocurrent. Indeed, the simple thermal

agitation of the electrons at room temperature causes parasitic electronic transitions, thus creating electron / hole pairs; it is the phenomenon of thermal generation of the charge carriers. This results in a current known as the dark current, which flows through the detector in the absence of incident radiation. This problem is mainly due to the small gaps in the semiconductors used for detecting IR photons. There are a variety of dark current components, such as diffusion, Shockley-Read-Hall (SRH), trap assisted tunneling, band to band tunneling and surface leakage current, which are detailed in chapter 2.

These sensors are therefore costly because of the need for cooling which imposes constraints in terms of weight and power, but also because of the manufacturing processes and materials used.

1.4. Figure of Merits

This part is devoted to highlighting the many merit criteria for evaluating the performance of IR detectors.

1.4.1. R_0A Product and Dark Current

R_0 is the measured resistance value without applying bias to a detector and A is the detector area. R_0A (Ω-cm^2) is a parameter that makes it possible to evaluate the quality of the photodetector [9]. This product by the simple measure of resistance at zero voltage and by the simple knowledge of the surface area of the detector makes it possible to inform the order of magnitude of the dark current. This product is given by:

$$R_0.A = n\frac{k_BT}{qJ} \qquad (1.1)$$

where J is the current density and n is the ideality factor which is unity for an ideal photodiode limited by diffusion. Recall that in this diffusion regime the dark current is proportional to n_i^2. The product R_0A is therefore inversely proportional to n_i^2. In the case of a photodiode limited by the generation recombination mechanism (SRH), the product R_0A will therefore be inversely proportional to n_i (Figure 1.6).

Equation (1.1) shows a figure of merit inversely proportional to the dark current. Thus a simple resistance measurement at the zero voltage provides an approximate value of the dark current of the detector.

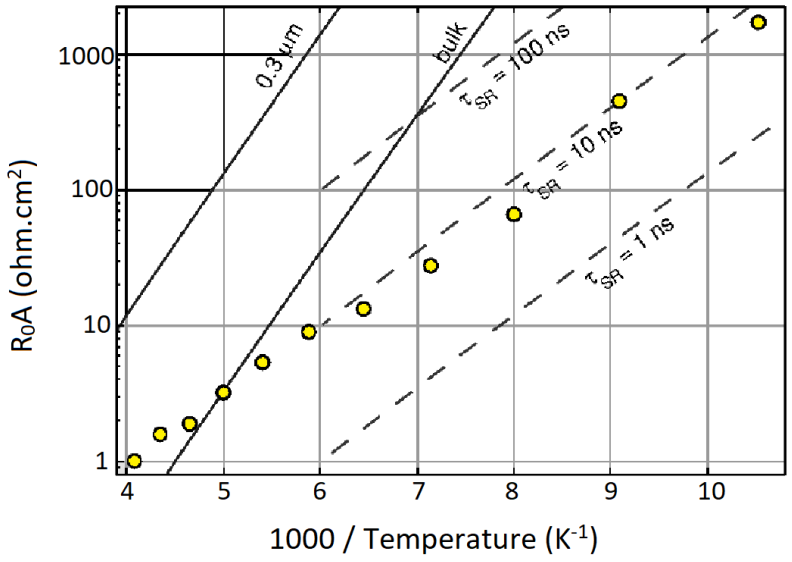

Figure 1.6: Evolution of the product R_0A as a function of temperature for both diffusion and generation-recombination regimes (redrawn as in the ref [8])

1.4.2. Quantum Efficiency and Spectral Response

The spectral response of a detector denoted R is defined as being the constant of proportionality between the signal coming from the detector and the incident light power P (λ) [10]. This power expressed in Watts and given by:

$$P(\lambda) = \frac{hc}{\lambda}\phi(\lambda) \qquad (1.2)$$

where ϕ is the incident photon flux at a given wavelength (λ). The spectral response in the case where the detector is a photodiode whose signal is a current I_{ph} is given by:

$$R_I(\lambda) = \frac{I_{ph}(\lambda)}{P(\lambda)} \qquad (1.3)$$

This magnitude expressed in A/W reflects the ability of a detector to respond to an incident light as a function of its wavelength. The spectral response is also related to a quantity called quantum efficiency. This efficiency defines the ratio of the generated

number of electron / hole pairs to the number of incoming photons and is equal to the 1 if each incident photon leads to the generation of a contributing electron [10]. It is given by:

$$\eta(\lambda) = \frac{I_{ph}(\lambda)}{q.\phi(\lambda)} \qquad (1.4)$$

1.4.3. Noise Current

Unwanted fluctuations in the measured signal are defined as noise. There are various noise mechanisms for detectors such as shot noise, 1/f (pink) noise and Johnson noise.

1/f (pink) noise: The 1 / f noise is an excess noise that was initially observed by Johnson [8]. The latter had found that the flow of a current in a resistive device was accompanied at low frequency by a noise whose spectral density is inversely proportional to the measurement frequency. This noise called pink noise or 1/f noise or flicker noise. It can be found in almost all systems. In photodetectors, considerable 1/f noise occurs. The noise spectrum equation can be written as:

$$S(f) = \frac{c}{f^{\alpha}} \qquad (1.5)$$

Where α is a number (between 0 and 3), c is a constant, and f is frequency.

Shot noise: The crossing of a potential barrier by a charge carrier is a random process causing the noise of shots also called Schottky noise. It is important for low level currents. A bias voltage needs to be applied to generate shot noise. This is main difference with respect to Johnson noise. The shot noise is given by:

$$i^2_{n_{shot}} = 2q(I_{dark} + I_{photo})\Delta f \qquad (1.6)$$

Johnson (Thermal) noise: It is caused by random movements of charge carriers whose temperature is bigger than 0 K. Their thermal energy increases as temperature increases.

$$i^2_{n\_johnson} = \frac{4kT\Delta f}{R} \qquad (1.7)$$

Device resistance is also important for Johnson noise level and Δf stands for measurement frequency bandwidth.

Total noise can be obtained through equation (1.8)

$$i_{total} = \sqrt{i_{n\_pink}^2 + i_{n\_shot}^2 + i_{n\_johnson}^2} \qquad (1.8)$$

1.4.4. Detectivity

The specific detectivity (D*) is the primary parameter that characterizes the performance of a detector through the standard signal-to-noise ratio of the photodetector [11]. This involves the current response and noise. A high performance detector is limited at low temperatures by shot noise (Equation 1.6). The specific detectivity in this case is written:

$$D^*(\lambda) = \frac{\lambda q}{hc}\eta(\lambda)\sqrt{\frac{A\Delta f}{2qI}} \qquad (1.9)$$

The specific detectivity is inversely proportional to the square root of the current. A photodiode is traversed by two types of currents: the photonic current (I_{ph}) constituting the useful signal and the dark current constituting the parasitic signal. When the current is dominated by the photocurrent, we speak of specific photon detectivity given by:

$$D_\phi(\lambda) = \frac{\lambda q}{hc}\sqrt{\frac{A\Delta f}{2}}\sqrt{\frac{n(\lambda)}{q^2\phi(\lambda)}} \qquad (1.10)$$

where I_{ph} is given by:

$$I_{ph} = q\eta(\lambda)\phi(\lambda) \qquad (1.11)$$

where, $\phi(\lambda)$ is the flux density at a specific wavelength.

In the case where the current is dominated by the dark current, we speak of specific dark detectivity given by:

$$D^2_{dark}(\lambda) = \frac{\lambda q}{hc}\eta(\lambda)\sqrt{\frac{A\Delta f}{2qI_{dark}}} \qquad (1.12)$$

The dark specific detectivity is no longer proportional to the square root of quantum efficiency as shown in equation (1.12), but becomes proportional to the efficiency itself. The relationship between these two detectivities gives:

$$\frac{D^*_{\phi}(\lambda)}{D^*_{dark}(\lambda)} = \sqrt{\phi_0(\lambda)/\phi(\lambda)} \qquad (1.13)$$

with

$$\phi_0(\lambda) = \frac{I_{dark}}{q\eta(\lambda)\phi(\lambda)} \qquad (1.14)$$

This flux value represents the limit between two regimes: the regime where the photonic current is mainly dominant and the regime where the dark current becomes predominant and strongly limits the operation of the detector.

1.5. Problems of High Operating Temperature Detection

1.5.1. High Dark Current Problem

All bodies, including detectors, radiate in a given spectral range, related to their temperature. To be able to perform its photo-detection function, the photodetector must imperatively be cooled in order to limit the thermal generation of the carriers. Any photosensitive device placed in the dark delivers a permanent current whose origin is attributed to various internal leakage mechanisms. This current, a function of polarization and temperature, is called dark current. Indeed, the measurement of the dark current shows that it increases considerably with the heating of the detector and therefore makes its use impossible at higher temperatures (Figure 1.7) [12]. When cooled, a high-performance detector is still limited by shot noise. This noise is due to random fluctuations of the electrons.

The need to operate these sensors at higher temperatures makes fundamental the study of physical mechanisms limiting the operation of photon detectors at high temperatures. Several avenues have been exploited: development of new growth techniques, development of sophisticated structures with abrupt composition profiles and complex doping profiles designed to allow operation at high temperatures. Indeed the deployment of heavy simulation means has made possible the design of these structures as well as their optimization for operation at higher temperatures. These HOT (High Operating Temperature) so-called third generation devices include several structures among which are cited: photon trapping structures, Auger suppression structures and barrier structures.

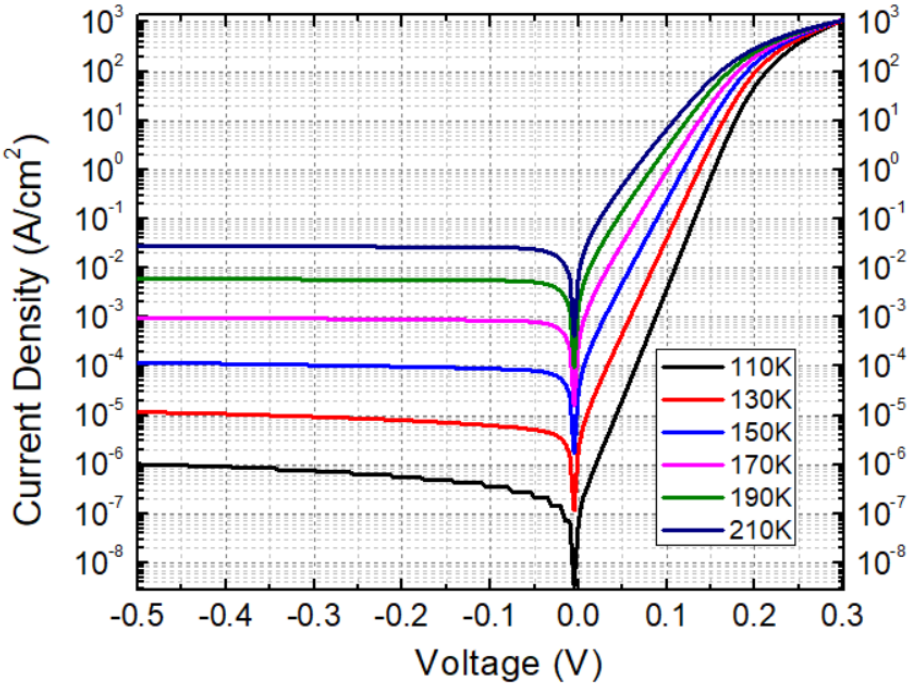

Figure 1.7: Current-voltage characteristics of a HgCdTe p-n photodiode at different temperatures

1.5.2. Operability Problems

Each photodiode corresponds to a pixel of a detection matrix hybridized to a readout electronics, which responsible for ensuring the bias voltage to photodiodes and processing of the measured signal from each of them in order to constitute the final image.

The signal-to-noise ratio (SNR) is used to evaluate the impact of noise on the final image. This ratio deteriorates as the detector heats up which quickly becomes limited by 1/f noise. A progressive increase in the operating temperature, shows that some pixels exhibit a 1/f noise well before the others. This behavior is manifested by a rate of defects which increases with temperature and which affects the quality of the final image.

Noise operability, which gives the percentage of pixels whose noise performance is within a confidence interval around the nominal value, deteriorates more and more with temperature. For HOT detection, understanding the different physical mechanisms contributing to the dark current and the 1 / f noise is therefore essential in order to develop detection structures having acceptable high temperature noise performance. The choice of material is also important. Indeed a good crystalline quality of the material can contribute to the reduction of the dark current and the noise 1 / f.

CHAPTER 2

HGCDTE PHOTOVOLTAIC PHOTODETECTORS

2.1. HgCdTe Based Infrared Detectors

In this section, FPAs based on the HgCdTe technology will be discussed. After the presentation of the structure of these detectors, HgCdTe material which is responsible for the detection process will be explained.

2.1.1. Architecture of the FPAs Based on a PN Junction

FPAs are detection matrices, which are consisting of essentially of two parts: the detection circuit and the readout circuit, as can be seen in Figure 2.1. These two circuits are interconnected electrically and mechanically by indium bonds through a hybridization step [13].

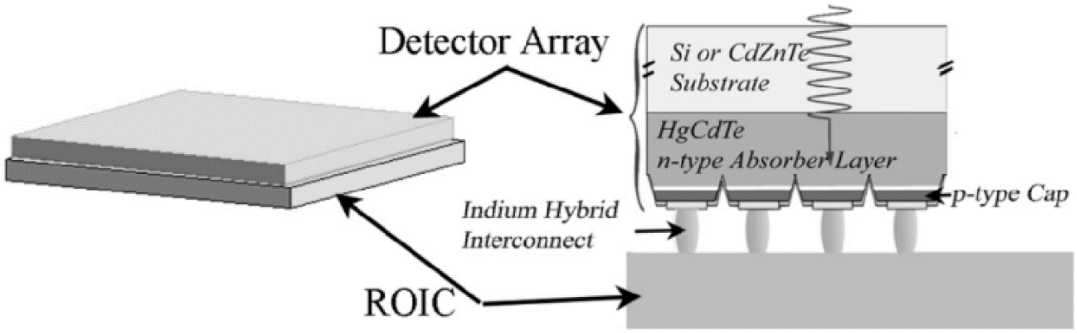

Figure 2.1: Schematic of a typical FPA Structure (redrawn as in the ref [13])

The detection circuit is composed of a multitude of elementary detectors formed by the p-n junction, which convert photons into electrons. Each elementary detector represents a pixel.

The readout circuit is usually made of silicon, and is in charge of converting the current (photonics and darkness) into a voltage measurable by the user [14-15]. In the

following, only the detection circuit will be described, since our objective is to improve photodiode performance at higher temperatures.

As shown in Figure 2.1, this circuit is composed of a stack of layers. The first is a substrate, such as CdZnTe, Si or GaAs [16], which serves as a support for the growth of the active layer of HgCdTe during manufacture. After passing through a possible anti reflection layer and the substrate, transparent in the IR, the photons are absorbed and generate a photocurrent in the absorber layer [17].

Generally, HgCdTe-based FPAs are cooled to a temperature between 200K and 220K for operation in the SWIR, between 80K and 120K for the MWIR domain, and between 50K and 80K for the LWIR [18 - 19].

2.1.2. Properties of HgCdTe

Since the first HgCdTe detector of Lawson et al. in 1959 [20], studies on HgCdTe have increased significantly, making it one of the most mature semiconductors used in thermal detectors.

HgCdTe is an alloy of CdTe (cadmium telluride) and HgTe (mercury telluride). It is part of the II-VI semiconductors because the atoms involved are on columns II (Hg and Cd) and VI (Te) of the periodic table of elements.

Its crystallographic structure is a so-called zinc blende structure, formed by two cubic, centric, interlocked, and diagonal-facing cubic networks, as shown in Figure 2.2. Each atom establishes covalent bonds with its four neighbors to form a massive crystallographic material. The crystal $Hg_{(1-x)}Cd_xTe$ contains Cadmium or Mercury atoms in the x proportion of Cd. This molar concentration will be called composition in the rest of the study. It will be shown that it adds a degree of additional freedom in the modeling of the detection process, unlike other materials used in the IR detection such as InSb.

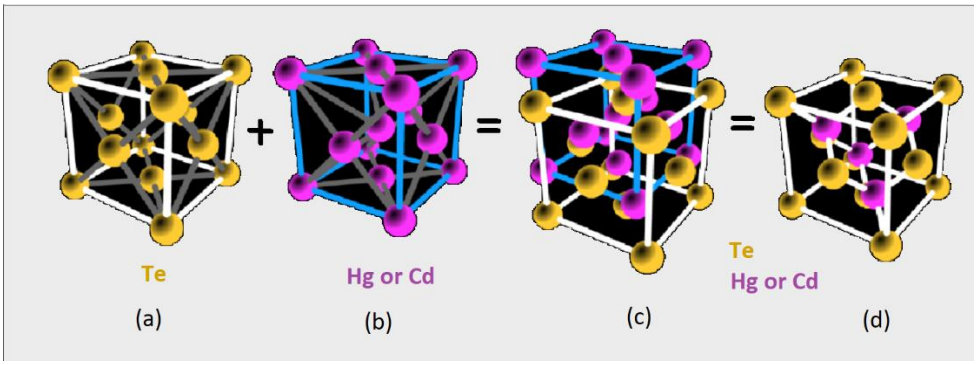

Figure 2.2: Schematic of (a) cubic face-centered structure of Te (b) cubic face-centered structure of Hg or Cd, (c and d) Zinc blende structure of HgCdTe (redrawn as in the ref [13])

The band structure is associated with the regularity of the crystal lattice, thus any error can cause a disturbance in the energy bands. This results in the presence of a large dark current and the creation of intermediate energy levels within the forbidden band, capable of allowing parasitic transitions of the electrons. This is why it is preferred to control the concentration of doping atoms, so that the perturbation of conductivity properties is better known, which makes it possible to better control the detection of IR photons. This process corresponds to the doping of the semiconductor, which is explained in the previous chapter (introduction).

After the growth of HgCdTe on the CdZnTe (Si or GaAs) substrate, the next step is to create p-n junctions to form the IR pixels. Among the numerous architectures of the HgCdTe-based p-n junctions, the p on n mesa structure is an example, represented in Figure 2.3. In the remainder of this study, a similar structure will be considered for comparison with the designed structure.

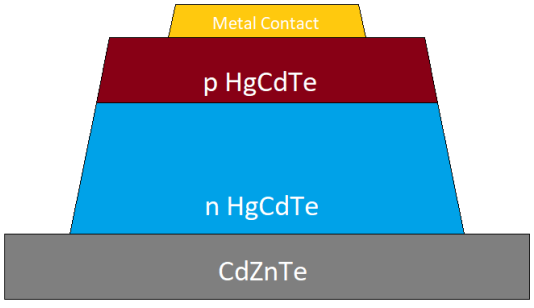

Figure 2.3: Schematic of a p-on-n mesa structure of HgCdTe

2.1.3. Energy Bandgap and Composition Relation in HgCdTe

The gap energy (E_g) of the material $Hg_{(1-x)}Cd_xTe$ can vary between 0.05 and 1.7 eV, depending on the cadmium composition (x), thus making it possible to cover a wide spectral range of detection between 0.7 µm and 25 µm [16].

In the current state of the art, the most commonly used formula for calculating the dependence of E_g on temperature T and on composition x is the empirical expression of Hansen-Schmit-Casselman (HSC) [21], given by equation 2.1 [18]. E_g and T are expressed in eV and K, respectively. It is valid for x between 0.2 and 0.6 and is illustrated in Figure 2.4.

$$E_g(x,T) = -0.302 + 1.93x - 0.810x^2 + 0.832x^2 + 5.35.10(-4).(1-2x)T \qquad (2.1)$$

The gap energy increases with temperature for Cd compositions below 50%, as shown in Figure 2.4. Beyond this composition, the temperature dependence changes, and the gap energy decreases with temperature. To explain these trends, it should be remembered that the HgCdTe material is an alloy between the CdTe and the HgTe whose gap energies are increasing and decreasing respectively, as a function of temperature. Thus, according to the Cd composition, the behavior of the gap energy of the HgCdTe will tend towards the majority behavior in the structure.

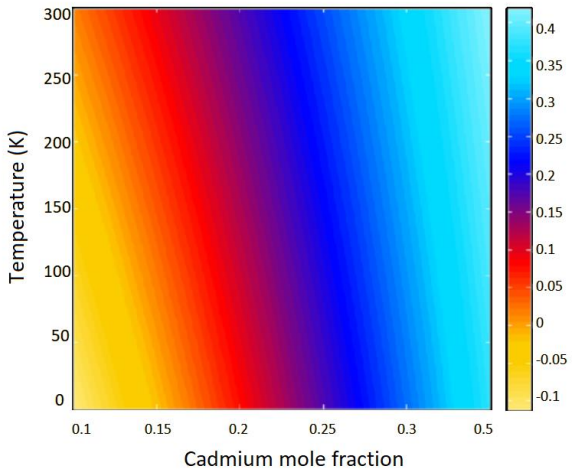

Figure 2.4: Bandgap of HgCdTe as a function of temperature and Cd composition (redrawn as in the ref [21])

2.1.4. Cut-off Wavelengths in HgCdTe

The notion of photon absorption coefficient in the process of radiative generation of carriers in the semiconductor is essential. Direct bandgap semiconductors such as HgCdTe have the particularity of having the maximum of the valence band coinciding with the minimum of the conduction band [22]. Therefore, the direct bandgap semiconductors are the most used in optoelectronics applications because they maximize the radiative processes.

In the direct bandgap semiconductors, the absorption profile is substantially the same. When photon energies are below the bandgap, the absorption is almost zero and the material is said to be transparent to radiation. On the other hand, if the incident photon energy is greater than the bandgap of the semiconductor, then there is absorption, and the absorption coefficient is constant [18].

In the literature, the cut-off wavelength (λ_c), which affects the optical absorption threshold of the semiconductor material, is the subject of several definitions. It is sometimes defined as being the wavelength related to gap energy, as shown in Equation (2.2) [18]. In this formula, h and c represent the Planck constant and the speed of light.

$$\lambda_c(\mu m) = \frac{hc}{E_g} = \frac{1.24}{E_g(eV)} \qquad (2.2)$$

Figure 2.5 contains information on cut-off wavelengths respect to Cd composition, where the gap energy E_g is computed with the HSC equation (see equation (2.1)) for two operating temperatures: 77K and 300K.

As shown in Figure 2.5, in the LWIR spectral range (around 12 µm), there is a very fast cut-off wavelength (λ_c) variation with the composition, which is less the case in the SWIR spectral range (< 3 µm). Therefore, to obtain acceptable cut-off wavelength uniformity in a HgCdTe-based FPAs, compositional control will be more critical for LWIR than for SWIR or MWIR [18].

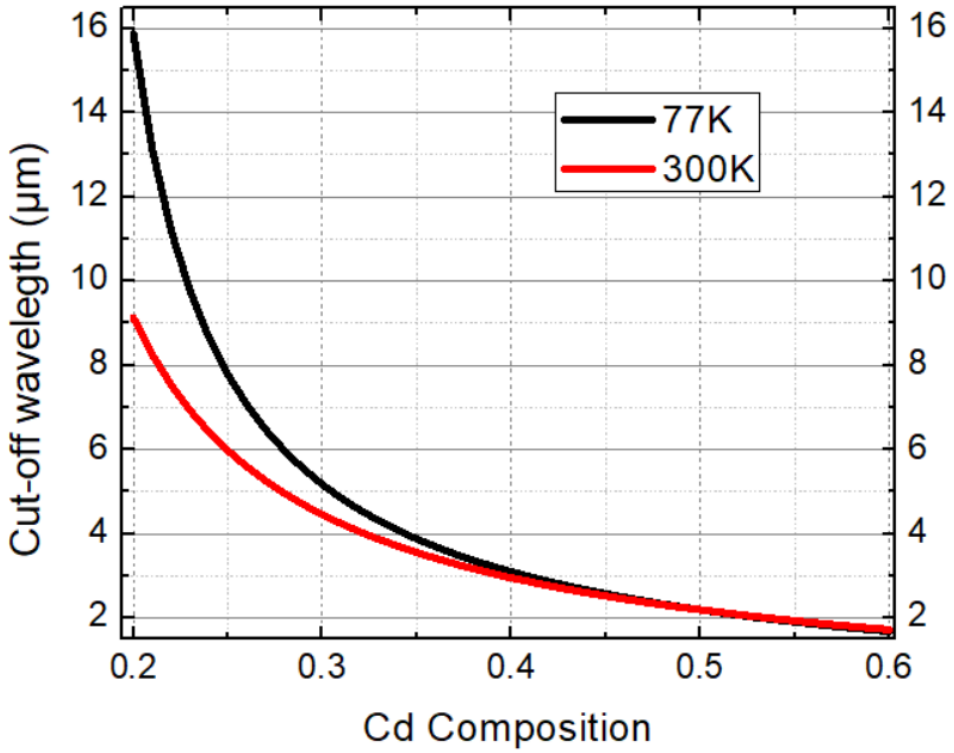

Figure 2.5: Cut-off wavelength of HgCdTe as a function of Cd composition

2.1.5. Recent Research in HgCdTe

The main lines of research on HgCdTe concern in particular the increase of the operating temperature. This allows a gain in energy consumption of the cooling system, while maintaining high performance especially in terms of noise and operability. The research axis on p-n architectures of the photodiode is also being developed, with the aim of reducing the dark current [23-24-25-26-27].

Increasing the format of the matrixes of transducers and the reduction of the pixel size are also tracks explored [28-29], intending to improve imaging performance. In addition, more and more work is being done on the use of silicon (or GaAs) [30-31] as an alternative to the CdZnTe substrate, which is historically used for HgCdTe growth, for cost reduction and better thermomechanical stability of the focal plane. Furthermore, improvements in the dual-band detectors [32-33] have also been made in recent years.

2.2. Recombination Mechanisms in HgCdTe

The lifetime of the photo-generated holes and electrons is one of the determining parameters in the evaluation of the performances of the HgCdTe detectors [34]. Therefore, it is crucial to develop a clear understanding and correct interpretation of the life of minority carriers and the mechanisms of recombination governing it.

The recombination of the electron / hole pairs can be done in two ways. The first is the direct passage of an electron from the conduction band to an unoccupied state in the valence band. This is a live tape process. The second is initially the transition of an electron from the conduction band to an energy level of an impurity acting as a "recombination center" located in the forbidden band to be reemitted thereafter to the valence band. This second mechanism is therefore an indirect process.

In the recombination process of the electron / hole pairs, an excess of energy equal to the difference between the energy of the electron and the energy of the hole is released. This energy can be emitted as a photon. In this case, the recombination is called radiative. Otherwise, this energy can be dissipated in the network in the form of phonons. A third possibility is that this energy can be transferred to a third mobile carrier. This process is called the Auger process. In this study, Auger recombination, radiative and SRH (Shockley-Read-Hall) mechanisms are explained.

2.2.1. Radiative Recombination

Radiative recombination is an intrinsic mechanism that involves the recombination of a hole in the valence band with an electron in the conduction band. A photon can be emitted through the excess energy as shown in Figure 2.6. This mechanism is of paramount importance in direct bandgap semiconductors like HgCdTe. In a nondegenerate semiconductor material, the radiative recombination rate at which holes and electrons are annihilated simultaneously is associated with the concentration of electrons in the conduction band and the availability of holes in the valence band.

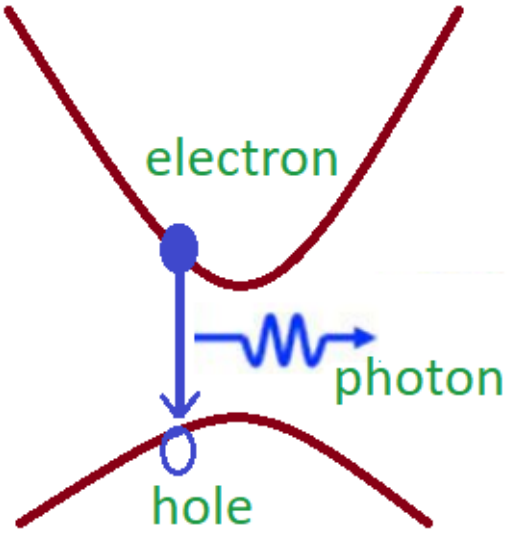

Figure 2.6: Schematic of radiative recombination in semiconductors (redrawn as in the ref [35])

The theory of radiative recombination was developed by van Roosbroeck and Shockley [35]. The expressions of the radiative lifetime and the recombination rate ($cm^{-3}.s^{-1}$) in HgCdTe presented below assume that the bands are parabolic and the semiconductor is non-degenerate:

$$R_{rad} = G_R(np - n_i^2) \qquad (2.3)$$

$$\tau_{rad} = \frac{1}{G_R(n+p)} \qquad (2.4)$$

where G_R is the capture probability given by [36]:

$$G_R = 5.8x10^{-13}\epsilon_\infty^{0.5}\left(\frac{m_0}{m_e^*+m_h^*}\right)^{1.5}\left(1+\frac{m_0}{m_e^*}+\frac{m_0}{m_h^*}\right)\left(\frac{300}{T}\right)^{1.5}E_g^2 \qquad (2.5)$$

with ε_∞ the high-frequency dielectric constant, m_e^* the effective mass of the electrons, m_0 the mass of the free electron, m_h^* the effective mass of the holes and E_g the gap energy expressed in eV.

As seen from the above equations, a similar radiative lifetime is expected for both the p and n type semiconductors.

The evolution of the radiative lifetime as a function of temperature is shown in Figure 2.7 at different doping concentrations (these results were obtained with Comsol Multiphysics). Through this evolution, it can be said that this mechanism can be important only for high doping. Note however that in the case of very high doping (> 10^{17} cm^{-3}) the small gap material quickly becomes degenerate.

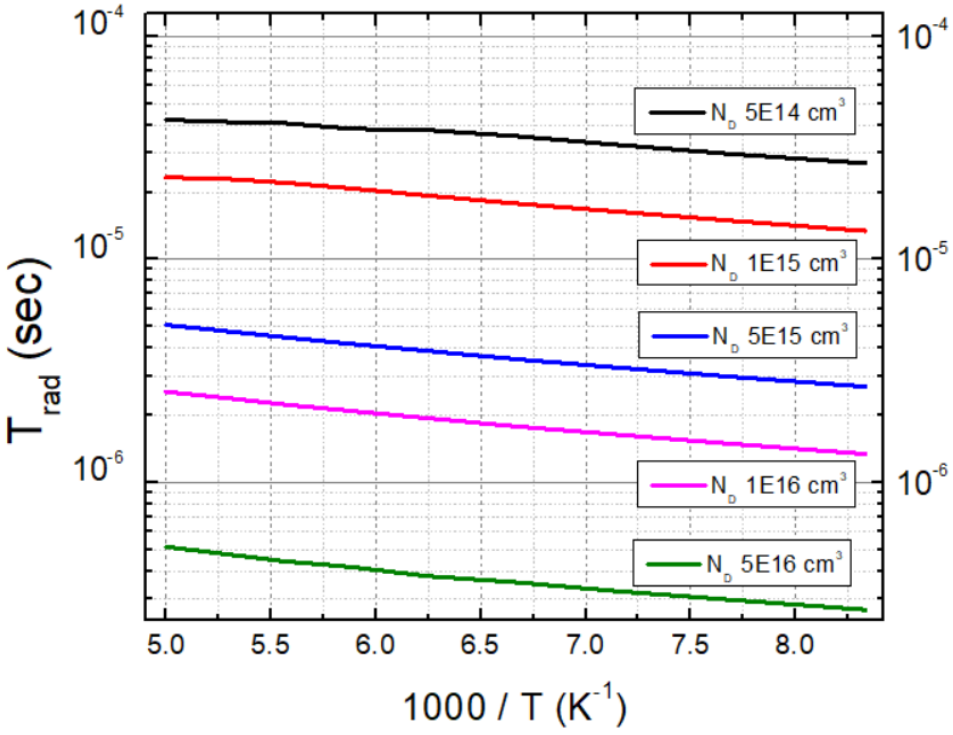

Figure 2.7: Radiative lifetime as a function of temperature for different doping concentrations in HgCdTe

2.2.2. Auger Recombination

It can be considered as the reverse process to carrier generation by impact ionization. Indeed this is an energy transition to third particle during recombination. When recombining an electron in the conduction band with a hole in the valence band, the released energy is transferred to another electron or other hole [37].

The main types of Auger mechanisms are shown in Figure 2.8: the Auger-1 and Auger-7 mechanisms [38]. The Auger-1 transition, illustrated by the left-hand diagram, and taking place in n-type materials, is defined by the recombination of a

minority carrier, the heavy hole in this case, with an electron in the conduction band, and another electron gains energy [39]. The Auger-7 transition occurs in a p-doped material, where a minority electron will recombine with a heavy hole in the valence band, and the conservation of energy and moments will lead to the creation of a light hole. This transition is illustrated on the right in Figure 2.8.

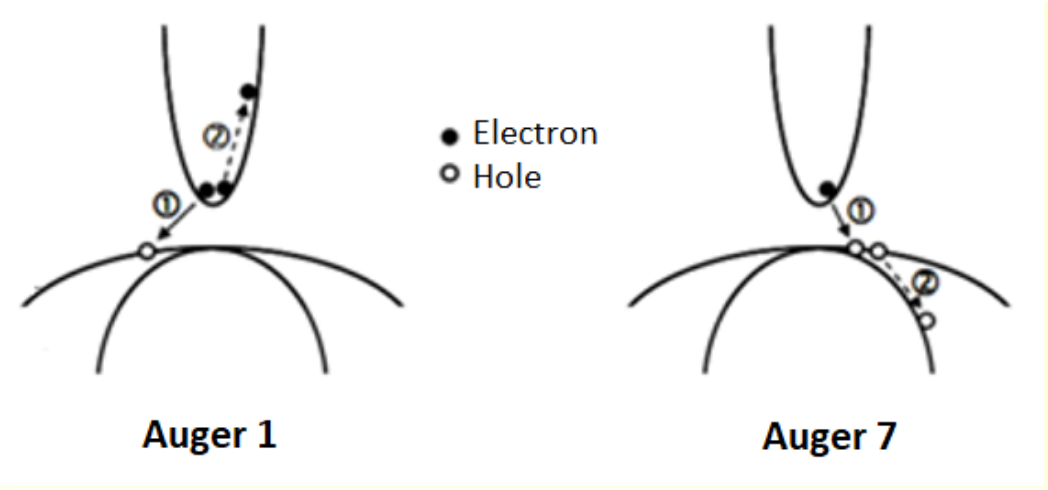

Figure 2.8: Schematics of Auger 1 and Auger 7 recombination (redrawn as in the ref [39])

Auger-1 lifetime

The Auger-1 lifetime for an intrinsic semiconductor is given by [40]:

$$\tau_{A1i} = 7.6x10^{-18}\epsilon_{\infty}^{2}\left(\frac{(1+\mu')^{0.5}(1+2\mu')}{\frac{m_e^*}{m_0}|F_1F_2|^2}\right)\left(\frac{E_g}{K_BT}\right)^{1.5}\exp\left(\frac{(1+2\mu')}{(1+\mu')}\frac{E_g}{k_BT}\right) \qquad (2.6)$$

where $\mu' = m_e^*/m_h^*$ is the ratio of the effective masses representing the dissymmetry of the bands, $|F_1F_2|$ indicates the overlap integral of the bands (between 0.1 and 0.3). This rather heavy expression has been simplified by Kinch for the HgCdTe and becomes:

$$\tau_{A1i} = 8.3x10^{-13}E_g^{0.5}\left(\frac{1}{K_BT}\right)^{1.5}\exp\left(\frac{(1+2\mu')}{(1+\mu')}\frac{E_g}{K_BT}\right) \qquad (2.7)$$

In the extrinsic regime, the Auger-1 lifetime is modified by the level of doping:

$$\tau_{A_1} = \frac{2n_i^2}{N_D(N_D+N_A)}\tau_{A1i} \qquad (2.8)$$

For an n-doped semiconductor, the Auger-1 extrinsic lifetime is inversely proportional to the square of the doping:

$$\tau_{A1} \propto \frac{1}{N_D^2} \qquad (2.9)$$

Thus, the Auger-1 mechanism limits the operation of the HOT diode for high doping values.

Auger-7 lifetime

The Auger-7 lifetime for an intrinsic semiconductor is usually expressed in terms of the Auger-1 lifetime. It is usually taken as a first approximation proportional to Auger-1 lifetime:

$$\tau_{A7i} = \gamma \tau_{A1i} \qquad (2.10)$$

where γ is an empirical parameter that varies from 12 to 60 [39]. The Auger-7 lifetime for an extrinsic semiconductor is thus deduced from equation (2.8) and is given by:

$$\tau_{A7} = \frac{2n_i^2}{N_A(N_D+N_A)} \gamma \tau_{A1i} \qquad (2.11)$$

The Auger-7 is the most common Auger mechanism in a p-type semiconductor and it shows dominance at low temperature. However, the Auger-1 mechanism is no longer negligible at higher temperatures and must, therefore, be taken into account in the expression of the Auger lifetime for a p-type semiconductor. Thus the Auger lifetime in a p material is generally written as the inverse sum of the Auger-1 recombination and Auger-7 recombination:

$$\tau_A = [\tau_{A1}^{-1} + \tau_{A7}^{-1}]^{-1} \qquad (2.12)$$

Note, however, that Auger-1 recombination can exist in the p material when the number of electrons is high enough. This case is only obtained in the intrinsic case or under illumination. Thus this approximation (equation (2.12)) is valid only because the material becomes intrinsic to the temperatures for which Auger-1 is no longer negligible.

2.2.3. Shockley Read Hall Recombination

This mechanism involves the recombination of the electron / hole pairs via the energy trapping levels (E_t) located between the conduction band and the valence band. Thus, this mechanism is not an intrinsic process. In this case, a photon is emitted with excess energy. These trapping levels in the HgCdTe may be due to dislocations or impurities. They can be introduced during the growth of HgCdTe, during sample processing or during post-growth annealing.

As recombination centers, trap levels trap holes and electrons and release them as generating centers. The generation and recombination rates depend on the nature of the center and its predominant occupancy state, as well as the local densities of these carriers in the valence and conduction band. The statistical theory of this recombination mechanism was first developed by Shockley and Read and Hall [41-42].

The SRH model considers that there is only one localized recombination center located at a level of energy and with a trap density N_t (cm^{-3}) much smaller than the density of the majority carriers. The basic mechanisms are shown in Figure 2.9. There are four possible transitions via the localized recombination center through which holes and electrons can be captured and re-emitted. The localized state can be either full or empty. If empty, it can capture an electron from the conduction band, as shown in Figure 2.9 (a), or it can emit a hole in the valence band, as shown in Figure 2.9 (d). Once it is filled, there are still two possibilities. It can emit the electron to the conduction band with an emission rate, as shown in Figure 2.9 (b), or capture a hole in the valence band, as shown in Figure 2.9 (c). SRH recombination therefore depends on the quality of the material. A high density of dislocations implies a high density of trap levels and therefore a low SRH lifetime. For low radiation intensities, this is given by [40]:

$$\tau_{SRH} = \frac{\tau_{n_0}(p+p_1)+\tau_{p_0}(n+n_1)}{n+p} \qquad (2.13)$$

with p_1 and n_1 the hole and electron concentrations of the trap and given by:

$$n_1 = N_c . \exp(-q \frac{E_g - E_t}{K_B T}) \qquad (2.14)$$

$$p_1 = N_v . \exp(-q \frac{E_t}{K_B T}) \qquad (2.15)$$

In Equation (2.13), τ_{p0} and τ_{n0} are the characteristic lifetimes of the holes and electrons related to the thermal velocities (v_{th}) of the charge carriers (cm / s), to the concentration in N_t recombination centers and to their capture cross section σ_n and σ_p (cm^2). They are given by:

$$\tau_{n_0} = \frac{1}{\sigma_n V_{th} N_t} \qquad (2.16)$$

$$\tau_{p_0} = \frac{1}{\sigma_p V_{th} N_t} \qquad (2.17)$$

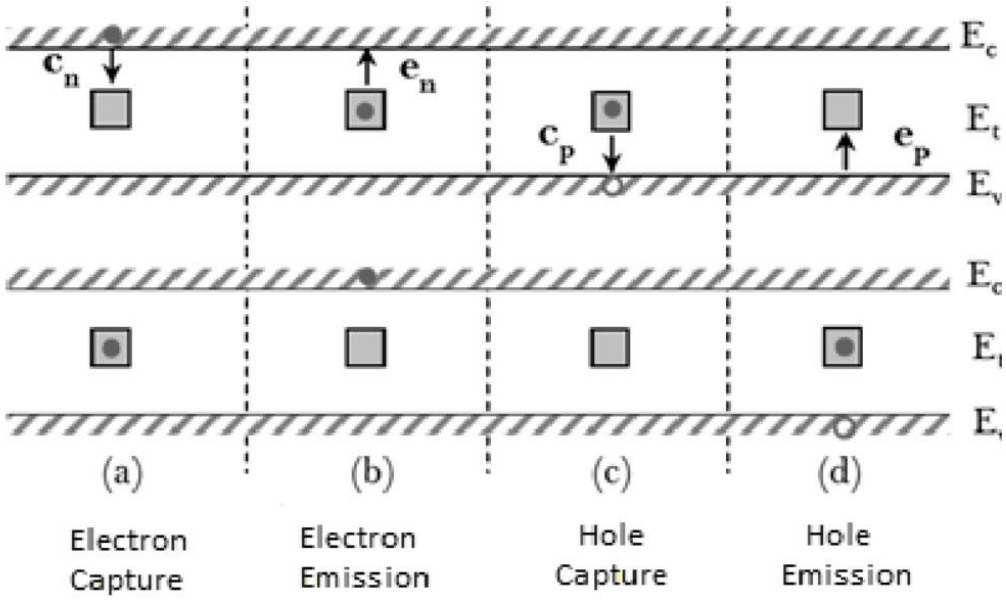

Figure 2.9: Schematics of SRH recombination mechanisms (redrawn as in the ref [43])

The SRH lifetime depends on the N_t (trap density) and E_t (energy of the trap level). Thus the SRH mechanism is a limit related to the quality of the material. So to summarize:

- The SRH (Shockley Read Hall) mechanism depends mainly on the quality of the material.

- The Auger-1 recombination mechanism is a mechanism whose lifetime is inversely proportional to the square of the doping. This mechanism is dominant in the n-type semiconductors and limits the operation of the more heavily doped IR photodiodes.

- The Auger-7 recombination mechanism is predominantly dominant in p-type semiconductors. However, the effect of the Auger-1 cannot always be negligible for high temperature operation.

- The radiative recombination mechanism rarely limits the operation of IR photodiodes since the photodiode is limited well before by the Auger mechanism.

The total lifetime of τ_{tot} carrier recombination is the combination of lifetimes induced by Auger, radiative and SRH recombinations. These contributions are added inversely to give total lifetime:

$$\frac{1}{\tau_{tot}} = \frac{1}{\tau_A} + \frac{1}{\tau_{rad}} + \frac{1}{\tau_{SRH}} \qquad (2.18)$$

2.3. Dark Current Components

The dark current results from the creation and displacement of electron-hole pairs, generated by thermal agitation and / or under the action of an electric field. It is associated with four phenomena: the diffusion of the thermally generated minority carriers, the band-to-band tunneling or the trap assisted tunneling, ohmic or common leakage currents and the generation-recombination in the space charge zone.

2.3.1. Diffusion Current

It is the ultimate limitation in a p-n junction photodiode. This current results from the diffusion of the minority carriers generated thermally near the depletion zone for a time corresponding to their lifetime [44]. During this characteristic period, these

carriers travel a so-called "diffusion length" distance corresponding to the depth of penetration of the minority. It is given by:

$$L_d = \sqrt{D\tau} \qquad (2.19)$$

where D is the diffusion constant defined by the Einstein relation:

$$D = \mu \frac{K_B T}{q} \qquad (2.20)$$

Note through these two equations that the diffusion length increases in the extrinsic regime with the temperature for a given lifetime. On the other hand, the lifetime and the diffusion length decrease very rapidly in the intrinsic regime.

In the case of an infinite material, the diffusion current density is given by:

$$J_{diff} = \frac{q n_i^2}{N} \frac{L_d}{\tau} \left(\exp\left(\frac{qV}{K_B T}\right) - 1 \right) \qquad (2.21)$$

In this equation “N” is the doping concentration of the semiconductor, not the intrinsic carrier density.

Equation (2.21) shows that the diffusion current is inversely proportional to the doping and the minority carrier lifetime. This equation also involves the intrinsic density of the carriers and therefore the density of the n or p minority carriers depending on whether it is a p-type and an n-type semiconductor. Indeed these two densities are connected by:

$$n_i^2 = n.p \qquad (2.22)$$

By replacing L_d by its expression in equation (2.21) we find another expression of the diffusion current:

$$J_{diff} = \frac{n_i^2}{N} \sqrt{\frac{q K_B T}{\tau}} \mu (\exp\left(\frac{qV}{K_B T}\right) - 1) \quad (2.23)$$

It can be seen from this formulation that the diffusion current is inversely proportional to the square root of the lifetime of the minority carriers and becomes proportional to the square root of their mobility.

Equation (2.21) is only valid for a material whose thickness is greater than L_d. In the case where one has to make thin layers of semiconductor, the diffusion volume is then no longer defined by the diffusion length (L_d) but rather by the thickness of the layer (e in equation). In this case L_d is replaced by in equation (2.21):

$$J_{diff} = \frac{qn_i^2}{N}\frac{e}{\tau_{diff}}\left(exp\left(\frac{qV}{K_BT}\right) - 1\right) \qquad (2.24)$$

The dark current induced by this diffusion regime is, to sum up, proportional to n_i^2, which depends exponentially on the bandgap of the semiconductor and the temperature (n_i α exp(-E_g / 2.K_B .T). Therefore, n_i increases exponentially with bandgap shrinking. Furthermore, the dark current of the detector is rather limited by diffusion at high temperature. It is, in fact, this exponential dependence on temperature that justifies the need to cool the detector in order to limit the thermal generation of the carriers. The J_{diff} (dark current) induced by the scattering regime also depends on the doping and displays different dependencies on the minority carrier lifetimes, oriented by the geometry of the structure [45]. In the case of a thick structure, this current is inversely proportional to the lifetime of the minority carriers (1/τ) and inversely proportional to their square root in the case of a fine structure (1 / √τ). The lifetime of the minority carriers is thus a key parameter for the dark current when the photodiode is limited by diffusion, which is generally the case at high temperature. For HOT operation it is therefore essential to have long lifetimes for reduction in the dark current.

2.3.2. Generation Recombination Current

Generation-recombination (G-R) mechanisms have a direct influence on the performance of IR detectors. The G-R current corresponds to the thermal generation

of the holes and electrons in the depletion zone and their drift in opposite directions due to the strong electric field which creates a current. When the electrons and the holes generated reach respectively the p and n side of the junction, they recombine and become majority carriers. The current corresponding to these G-R mechanisms can be given by:

$$J_{G-R} = q\frac{w}{2\tau_{G-R}}n_i\left(exp\left(\frac{qV}{K_BT}\right)-1\right) \qquad (2.24)$$

Equation (2.24) shows that the G-R current is proportional to the width of the space charge region (depletion region) and therefore to its volume and inversely proportional to the lifetime of the minority carriers. These lifetimes are associated with recombination mechanisms of the electron-hole pairs through energy trapping levels which are located between the valence band and the conduction band. Note also through equation (2.24) that the dark current induced by this G-R regime is proportional to n_i and not to n_i^2 as we have seen in the diffusion regime. Thus, in high-performance infrared photodiodes, the dark current is generally dominated by generation-recombination current at the low temperature and dominated by the diffusion current at higher temperature.

2.3.3. Tunneling Current

When the energy level occupied by the p-side conduction band becomes greater than that occupied by the n-valence band, minority carriers can easily pass from one side to other side. The tunneling current is divided into two categories depending on the mode of the passage of the minority carriers from one side to the other of the junction: the trap-assisted tunneling (TAT) and the band-to-band tunneling (BBT).

Band to Band Tunneling

In high reverse bias case, the minority carriers pass directly from one band to the other on both sides n and p of the tunnel junction (Figure 2.12): this is the band-to-band tunneling (BBT). This current contribution is all the more important as the temperature is low since the bandgap energy of the alloy $Hg_{(1-x)}Cd_xTe$ decreases with the

temperature for x ≤ 0.5. At a given temperature, this contribution increases when the cadmium composition decreases for the same reason. The expression of the tunneling current is deduced from the calculation of the probability of passage of the carriers through a triangular barrier and is given by:

$$J_{BBT} = A_1 EV \exp(-\frac{B_1}{\epsilon}) \qquad (2.25)$$

and

$$A_1 = \frac{q^3}{4\pi^2\hbar}\sqrt{\left(\frac{2m_e^2}{E_g}\right)} \qquad (2.26)$$

$$B_1 = \frac{4}{3q\hbar}\sqrt{2m_e^* E_g^3} \qquad (2.27)$$

This direct tunneling current depends exponentially on E field in the depletion region, the effective carrier mass and the bandgap of the semiconductor.

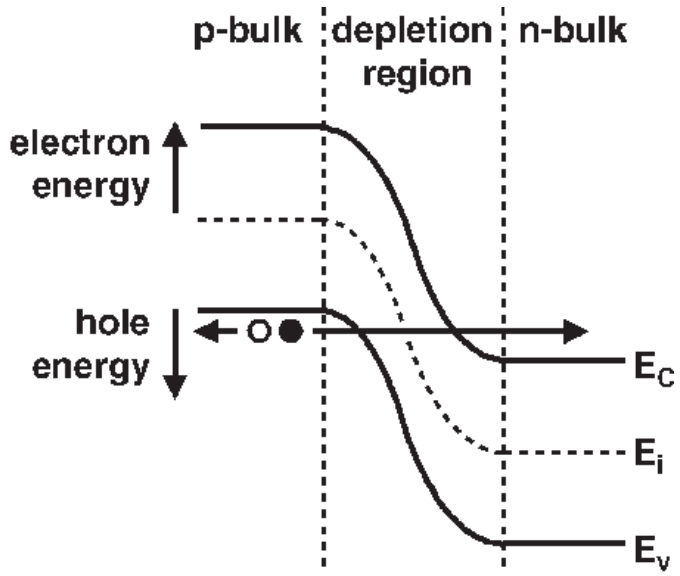

Figure 2.10: Schematic representation of band-to-band tunneling effect (redrawn as in the ref [8])

Trap Assisted Tunneling Current

The presence of traps (defects in the crystal lattice) in the depletion zone associated with the existence of an electric field makes it possible to tunnel the electrons of the

valence band to the level of the traps (E_t) and the level of the traps to the conduction band. This contribution to the dark current is called Trap Assisted Tunneling (TAT) and will intervene for lower reverse bias voltages than BTB. The temperature and polarization dependence of this transition may be different depending on the level of the traps (E_t) and their occupancy rate. The trap-assisted tunnel current is given by [5]:

$$J_{TAT} = qN_tWW_cN_c \qquad (2.28)$$

where W_cN_c is the probability of passage through tunnel effect.

Equation (2.28) uses trap density (N_t) and width (W) of the depletion region. The tunneling current is modulated by the width of the depletion region and therefore by the E prevailing field and depends on the quality of the material. Thus, a high quality crystalline material will limit the contributions of trap assisted tunneling current.

To sum up, the tunneling currents believe exponentially with the electric field of the space charge region, depending on the applied bias. They thus represent a limit for the small gap materials used in IR detection and particularly in the case of very long wavelength photodiodes.

2.3.4. Surface Current

The crystalline quality of the material and the state of the interfaces are two key parameters in the recombination mechanisms of the charge carriers and guide their life. Good interface quality and a good material significantly reduce the generation-recombination phenomena within the crystal and allow to obtain long lifetimes. Indeed, a high density of interface states is carrier generation source, collected by the junction will contribute to the dark current if especially the recombination rate at the interface is important. These carriers generated at the interface are proportional to the intrinsic density and carriers and the recombination rate at the interface (V_s), proportional to the density of traps N_t.

$$J_s = q\frac{n_i}{2}V_S \qquad (2.29)$$

CHAPTER 3

HIGH OPERATING TEMPERATURE STRUCTURES

The increased development of HgCdTe growth techniques and the fabrication of different detector structures have led to achievement of BLIP (background limited infrared photodetection) performance at high temperatures. The dark current of the photodetector which is proportional with temperature usually determines the maximum operating temperature. Recently, crucial improvements have been made in IR technology through material growth and device design innovations. In this chapter, three main high operating temperature structures will be explained.

3.1. Barrier Structure

At low temperatures the dark current of the detectors is limited by the generation-recombination current, then by the diffusion current at higher temperatures. However, the contribution of G-R mechanisms to dark current should not be excluded at high temperatures. From this observation came the idea of designing structures whose electric field is confined in a large bandgap material in order to limit the G-R mechanisms (SRH current) [46-47-48]. However, care must be taken that this large gap barrier does not hinder the transport of holes (in the case of nBn structure) on the valence band to ensure correct quantum efficiency. In other words, zero valence band offset is the most important issue in barrier detectors [49-50-51-52].

Barrier detectors offers several advantages over a conventional photodiode based on the p-n junction. These advantages are achieved by a significant reduction of depletion currents and surface leakage currents. In the scope of this thesis study, the following structure (Figure 3.1) was simulated with Comsol Multiphysics [53-54]. This structure is constituted as follows: a small gap absorber layer where the photogeneration will take place, a large gap barrier for filtering the majority carries and a contact layer

generally heavily doped to obtain the ohmic contact. The absorber layer is about one to two times the optical absorption length to ensure good quantum efficiency [55-56]. The thickness of the barrier is between 50 and 200 nm to limit the passage of electrons by tunnel effect. The thickness of the contact layer is generally of the order of a few hundreds of nanometers. HgCdTe was used in all layers and cadmium compositions were shown in Figure 3.1.

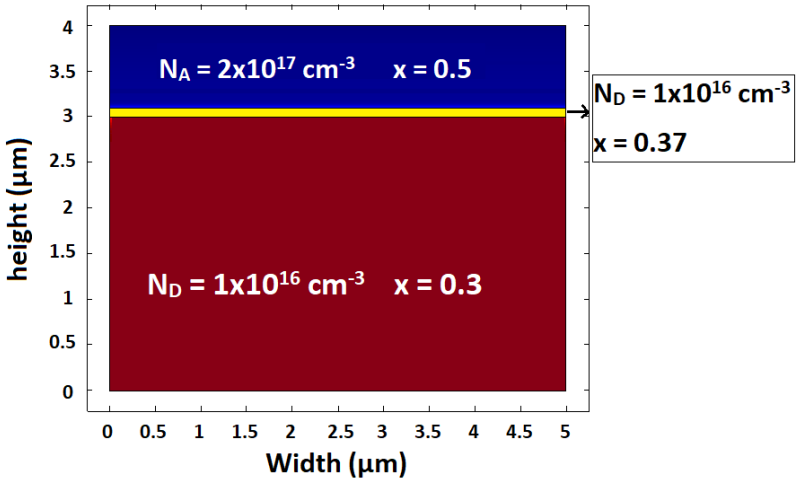

Figure 3.1: Simulated barrier structure

The energy band diagram of the simulated barrier structure is shown in Figure 3.2. Valence band discontinuity is about 19 meV. The quantum efficiency of the barrier structure drops almost 2% due to this discontinuity.

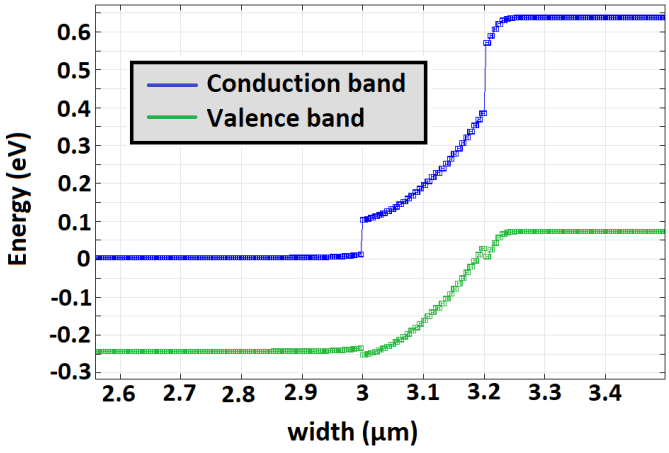

Figure 3.2: Energy band diagram of the simulated barrier structure

Temperature versus current density simulation results are also available in Figure 3.3. In the barrier structure, the SRH component of the dark current is completely removed at low temperatures. Applied bias is -0.1 V.

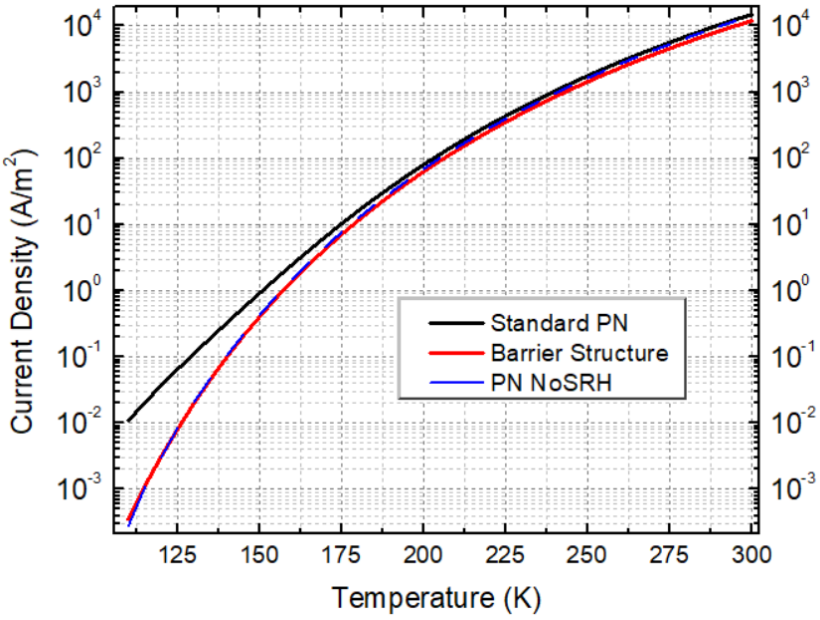

Figure 3.3: Current density vs temperature for the barrier structure, a standard p-n junction and a standard p-n junction (SRH component not included)

Shockley-Read-Hall recombination mechanism in the depletion zone involves the recombination of the electron-hole pairs via the energy trapping levels. These trapping levels are located between the valence band and the conduction band constitutes a major source of contribution to the dark current, especially at low temperatures. This source of depletion current is, on the other hand, minimized if the depletion is maintained in the large gap material of the barrier [24-57-58] as mentioned before. This concept has been exploited in the HgCdTe MWIR detectors where the issue of HOT has always been topical.

In 2015, N. D. Akhavan et al. [47] conducted a simulation study to compare different barrier structures, which are shown in Figure 3.4. SRH, Auger, BTBT, TAT and radiative components of the dark current were included in calculations. SRH lifetime was taken as 1 µs in this study. Trap density level was 0.25Eg and trap concentration was taken $5x10^{13}$ cm^{-3}. The thickness of the absorber layer was used 10 µm in MWIR

spectral range (x_{abs} = 0.3). The thickness of the barrier layer was 50 nm and the cadmium mole fraction was 0.6.

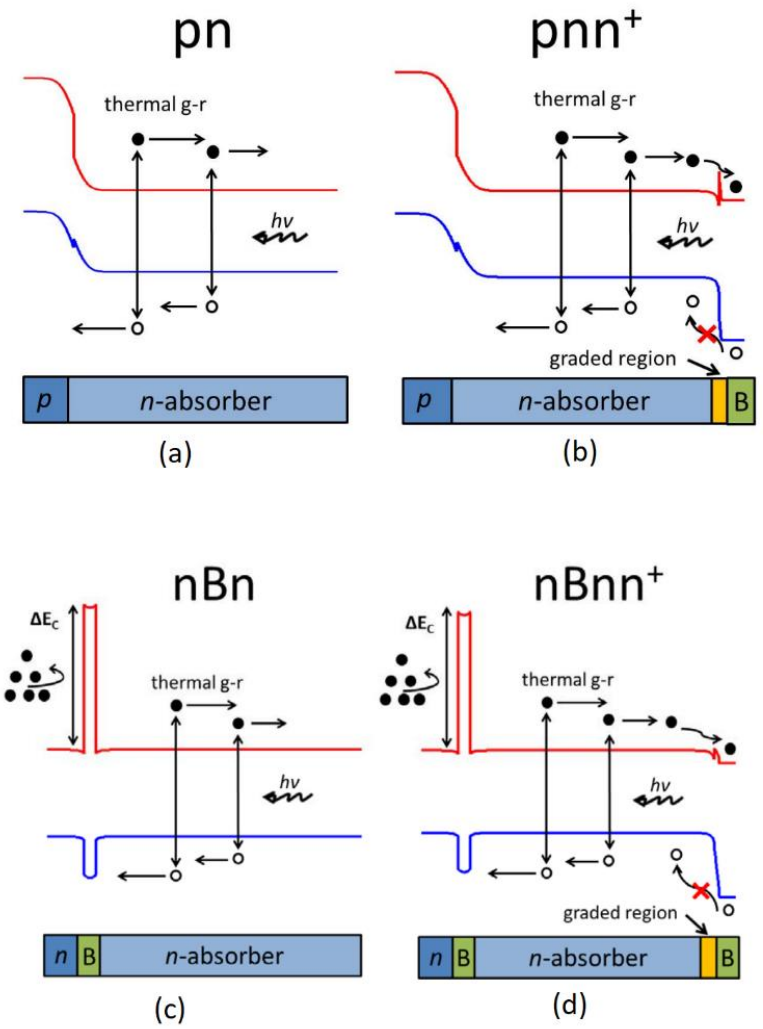

Figure 3.4: (a) Energy band diagrams of (a) a p-n photodiode (b) a HOT pnn$^+$, (c) a HOT nBn, and (d) a HOT nBnn$^+$ (redrawn as in the ref [47])

Simulations were performed at 300 mV reverse bias and the absorber doping level was taken 1x10^{15} cm^{-3}. The calculated dark current is shown in Figure 3.5. Especially at low temperatures, the reduction in the dark current appears in all barrier structures except pnn$^+$ (due to strong BTBT below 100 K). The closest structure to rule-07 is nBnn+. Another advantage of this structure is the absence of p-type doping, which provides great convenience during fabrication and growth.

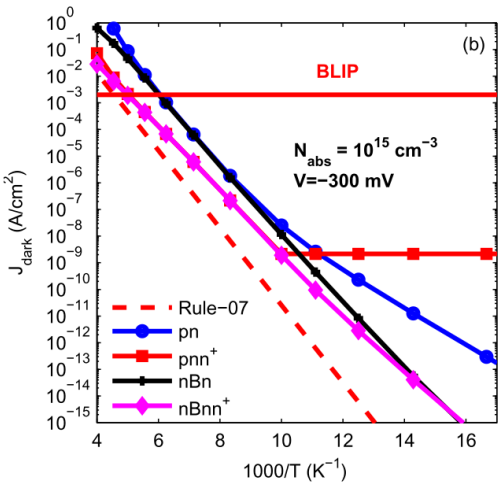

Figure 3.5: Dark current of the simulated HgCdTe photodiode as a function of temperature (redrawn as in the ref [47])

Another barrier study was conducted by A. Keblowski et al. in 2016 [58]. The main purpose of this study is to compare p-type and n-type absorber in barrier structures (Figure 3.6). The proposed structure was grown on 2″ GaAs substrate with MOCVD (Metal Oxide Chemical Vapor Deposition) and detector fabrication completed. The cut-off wavelength was adjusted to 3.6 µm at 230 K (x_{abs} = 0.36). Gold was used for metal contacts. In this structure, p-doping was carried out by arsenic implantation and n-doping by incorporation of indium during growth.

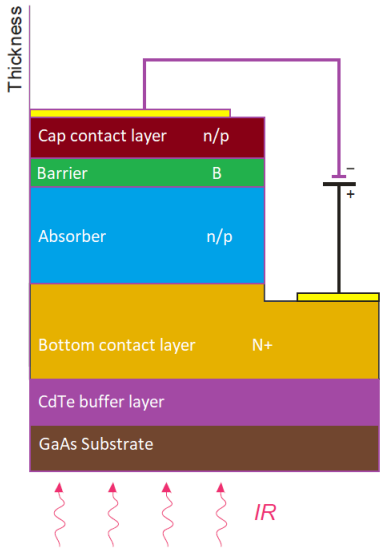

Figure 3.6: Schematic of a MWIR HgCdTe Mesa Structure (redrawn as in the ref [58])

In Figure 3.7, measured dark current values are shown as a function of temperature for pB_ppN and pB_pnN detectors. The same figure also includes the measured dark current-voltage graph for different temperatures. Comparing current levels at the same temperature shows that the n-type absorber exhibits less dark current than the p type absorber below 230 K.

In this study, from the dark current measurements, thermal activation energy was estimated to be 0.265 eV and 0.328 eV for p-type and n-type absorbers, respectively. This indicates that SRH behavior is present in the p-type absorber. On the other hand, the dark current appears to be limited to the diffusion current in the n-type absorber.

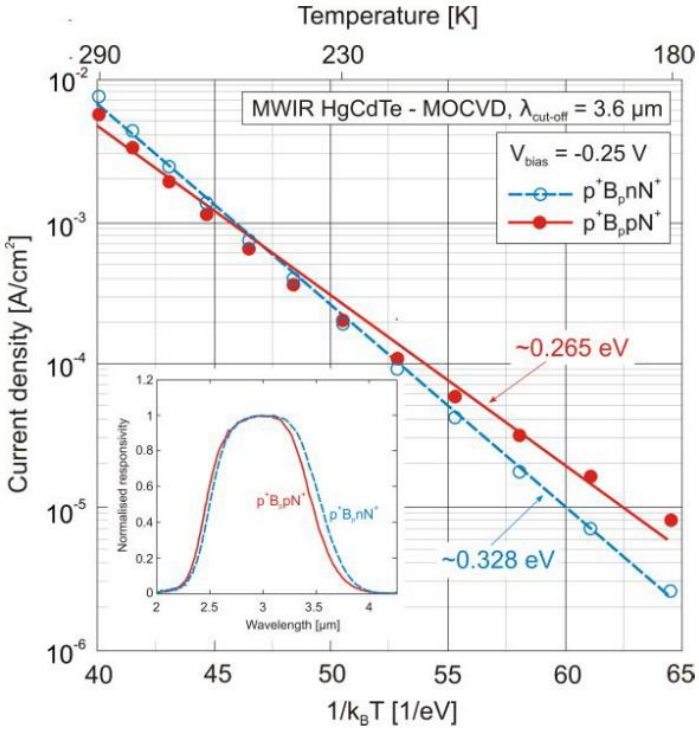

Figure 3.7: Measured dark current density at 0.25 V reverse bias as a function of temperature (redrawn as in the ref [58])

3.2. Auger Suppression Structure

Auger processes affect the performance of HgCdTe infrared detectors at near room temperatures of operation. Auger suppression structure is one way to eliminate this issue. This device structure was first proposed by Elliott and Ashley [59]. The main

device consists of a two terminal excluded/extracted. The absorber region of the device is near intrinsic and is π−type (lightly doped p-type) or ν−type (lightly doped n-type).

The minimum controllable doping is about mid-10^{14} cm^{-3}. On the other hand, the intrinsic carrier concentration is very high at higher temperatures in HgCdTe. It can reach values as high as 10^{15} cm^{-3} (Figure 3.8), which is higher than the actual extrinsic doping level in auger suppression structure [60].

Auger current is directly proportional to the number of available holes and electrons, and so they cause large dark current in HgCdTe IR devices operated at high temperatures where the absorber layer is nearly intrinsic at equilibrium [61].

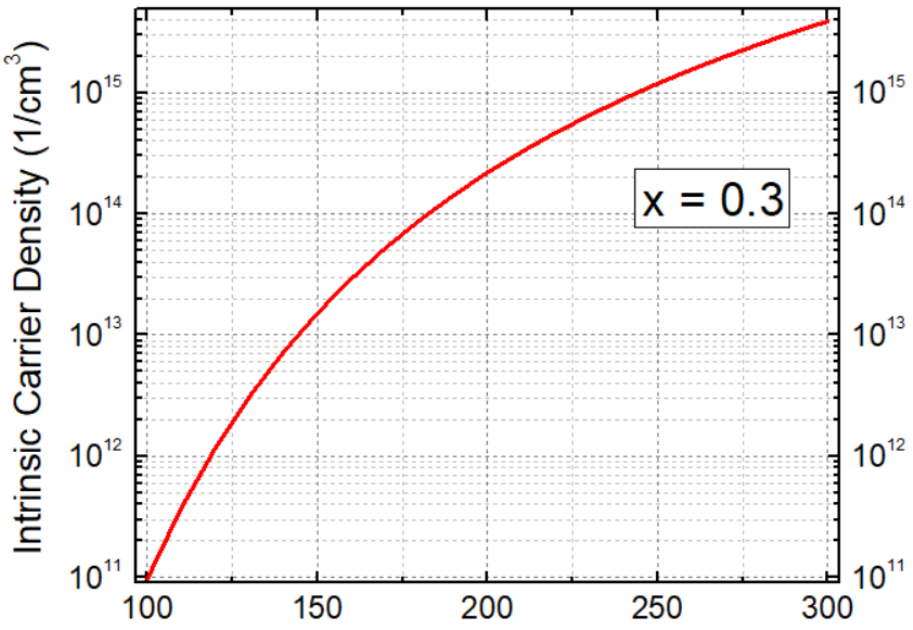

Figure 3.8: Intrinsic carrier density vs temperature in a typical HgCdTe

In the Auger suppression structure, the absorber layer is sandwiched between two layers that form the extracting and excluding contacts with the absorber layer. The N+/ν or P+/π heterojunction stands for the exclusion junction. The P+/ν or N+/π heterojunction stands for the extraction junction. For instance, when a P+/ν/N+ structure (Figure 3.5) operates at high temperature the absorber region ('ν' layer) is

intrinsic in thermal equilibrium. Fermi level lies in the conduction band in the case of highly n-type doped material (N+ region). Therefore, higher energy required to generate e-h pairs by Auger generation. Thus, hole concentration in the N+ region is decreased. Now, in the case of applying increasing reverse bias, the extraction junction (P+/ν) extracts the minority holes from the absorber region. However, hole injection from the N+ region will be slower in respect to extraction. Hence, the hole concentration in the absorber region drops below its thermal equilibrium value [62]. Then, the electron concentration also drops below the equilibrium value due to the charge neutrality rule.

When the applied reverse bias is increased, the electron concentration will eventually go from the intrinsic level (mid-10^{15} cm^{-3}) down to the extrinsic doping level (mid-10^{14} cm^{-3}) in the absorber region. This decrement in the hole and electron concentration provides significant reduction of Auger processes [63-64].

In 2011, Mohammad Nadimi and Ali Sadr simulated an HgCdTe medium-wave infrared detector with ATLAS (software from SILVACO) [61]. Their device structure is shown in Figure 3.9. The absorber layer of the structure is lightly doped ($1x10^{15}$ cm^{-3}). N^+ and p^+ layers are heavily doped ($1x10^{18}$ cm^{-3}).

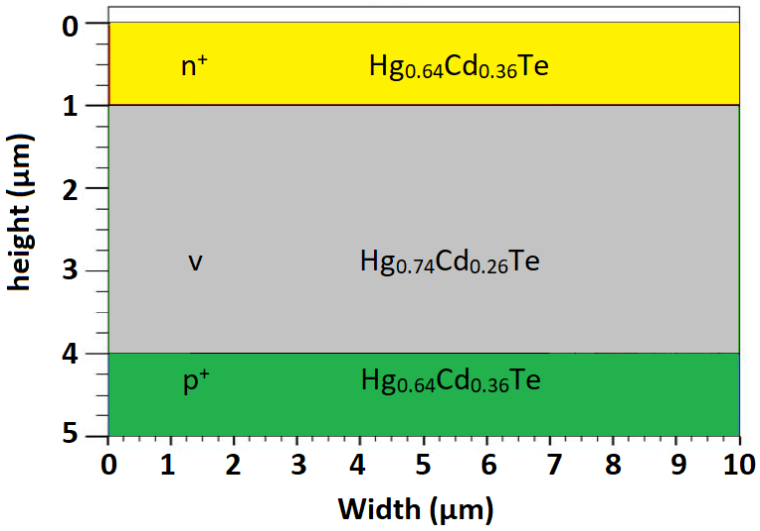

Figure 3.9: Schematic of Auger suppression structure (redrawn as in the ref [61])

The carrier concentration profiles of the Auger suppressed diode is shown in Figure 3.10 for equilibrium and under reverse-bias. From this result of the study, it can be seen that hole concentration inside the absorber region dropped by some order of magnitude and electron density also reduced to the below doping level (applied bias -0.35 V). This reduction in carrier density also leads to a reduction in dark current for high temperatures.

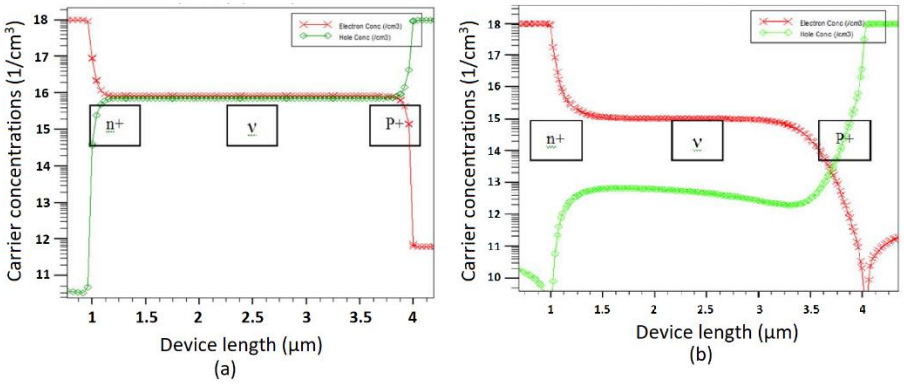

Figure 3.10: Carrier densities for (a) equilibrium and (b) non-equilibrium of the simulated structure (-0.35 V bias) (redrawn as in the ref [61])

Another similar study was done by S. Velicu et al [64]. The simulated structure also works in the MWIR spectral range ($x_{absorber}$ = 0.3). The p type doping of the top layer is $5x10^{17}$ cm^{-3} and n type doping of the bottom layer is $1x10^{17}$ cm^{-3}. Cadmium mole fraction of the N+ and P+ layers is 0.4. The band diagram is shown in Figure 3.11.

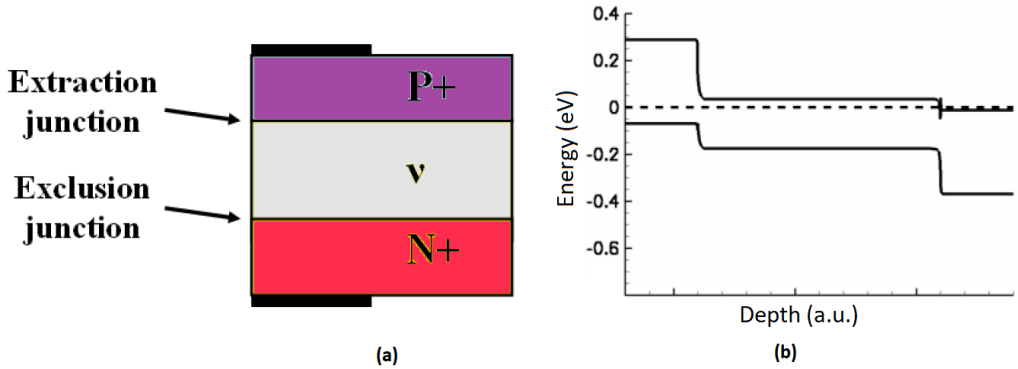

Figure 3.11: (a) Layer architecture and (b) energy diagram of the simulated HgCdTe structure (redrawn as in the ref [64])

In this study, simulations were done with Sentaurus software and results are compared with standard p-n photodiode structure (double layer heterojunction). In HOT devices the dark current is considerably smaller than DLPH. This leads to improvement in the detectivity (Figure 3.12).

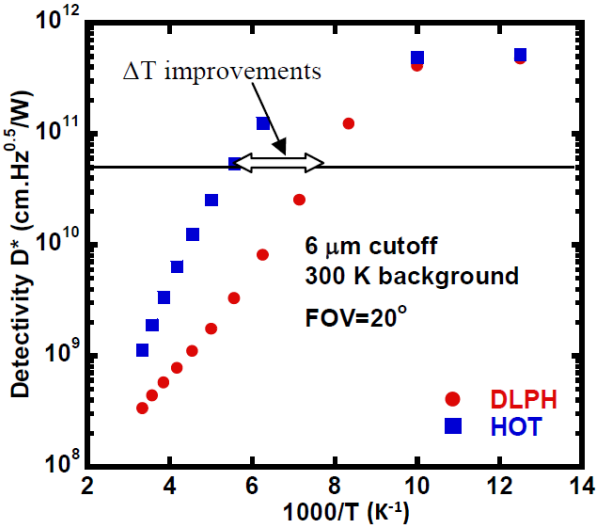

Figure 3.12: Detectivity of the simulated HgCdTe structure as a function of temperature (redrawn as in the ref [64])

In the scope of this thesis, the structure in the Figure 3.13 is simulated with COMSOL and detailed comparative results are shown here.

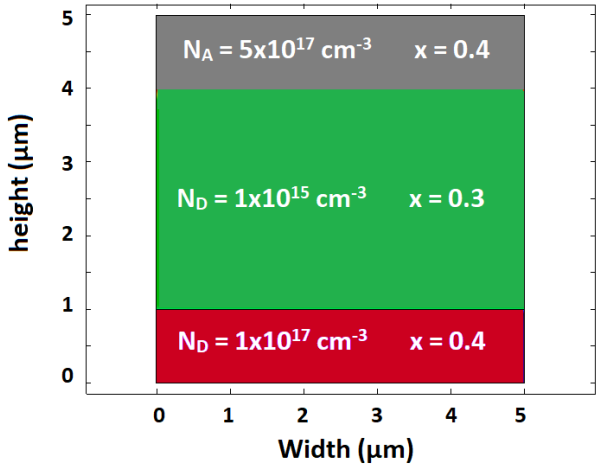

Figure 3.13: Layer architecture of the simulated Auger suppression structure

Firstly, a reduction in the Auger generation rate respect to applied reverse bias is calculated (Figure 3.14).

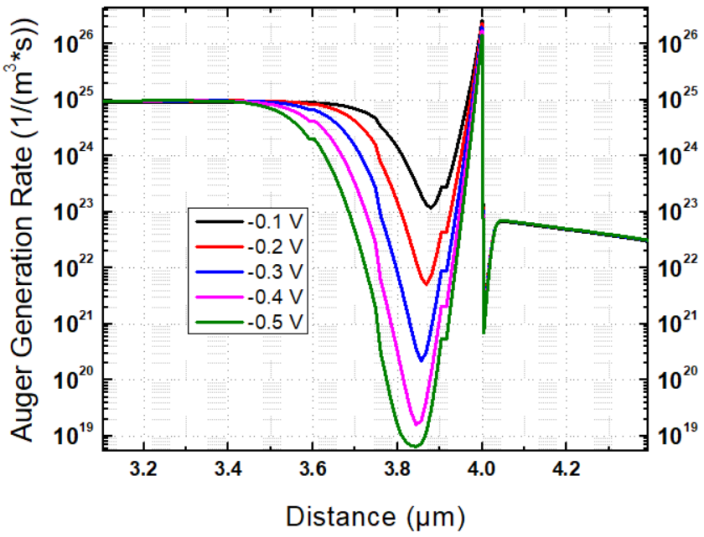

Figure 3.14: Auger generation rates in the simulated HgCdTe structure at different biases

Temperature versus current density simulation results are also available in Figure 3.15. In this structure, the Auger component of the dark current is completely removed at higher temperatures.

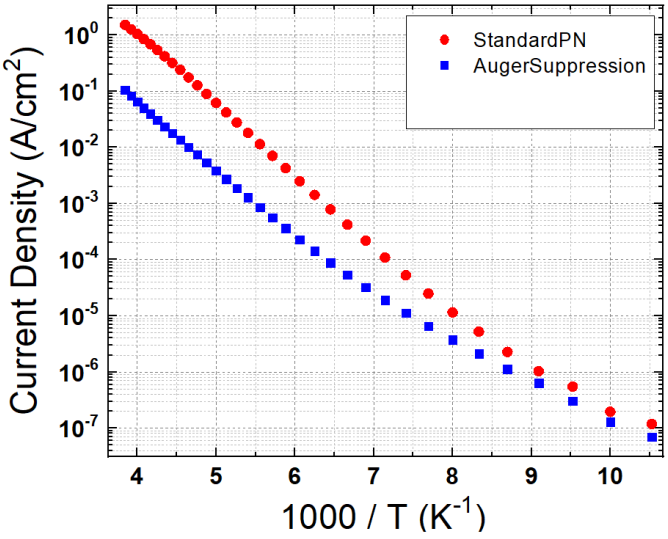

Figure 3.15: Current density vs temperature for Auger suppression structure and a standard p-n junction

For different temperatures, current-voltage graphs of the standard PN structure and Auger suppression structure are shown in Figure 3.16.

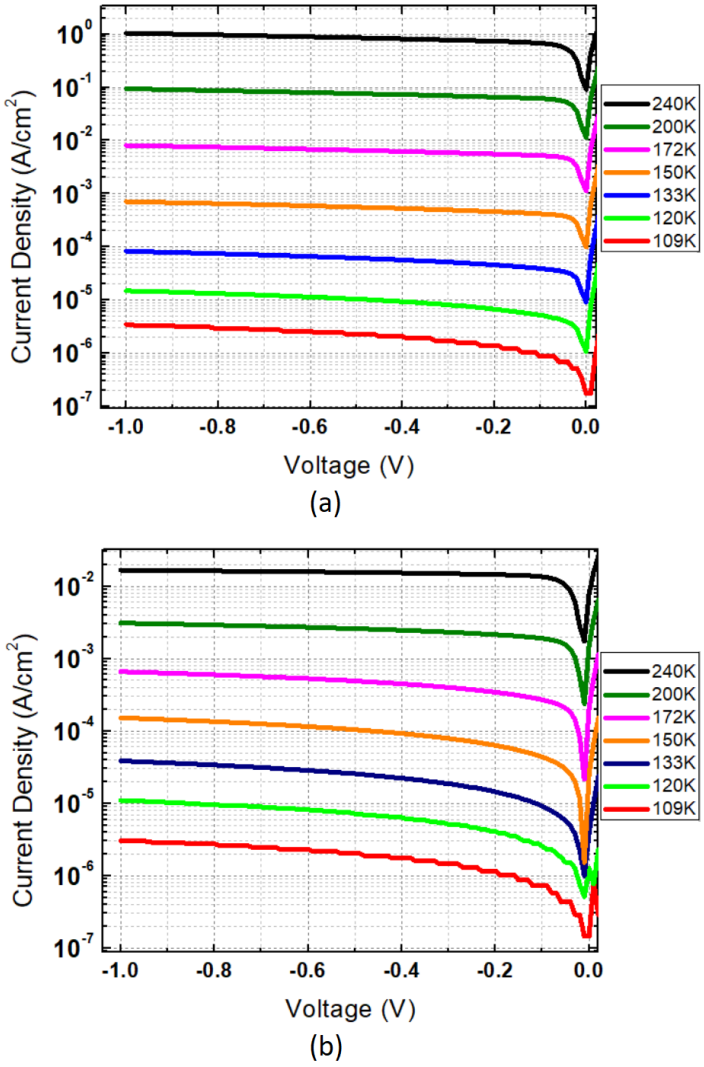

Figure 3.16: Current density - voltage graphs for (a) a standard p-n junction and (b) the Auger suppression structure

3.3. Photon Trapping Structure

Fill factor is an important concept for mesa structures in photovoltaic detectors. Decrement in the fill factor affects both the quantum efficiency and dark current [65]. To reduce dark current without dropping quantum efficiency, Wehner et al. have proposed the photonic crystal structure which is a kind of HgCdTe infrared detector

[66]. This study shows that proper design can provide the light be absorbed completely in the smaller effective regions, and thus maintain the quantum efficiency with reducing the volume of the device based on the modulated photonic field distributions in the photonic crystal structure. Furthermore, the detector dark current is dropped through the reduced volume of the material [67-68].

The trapping method is to perform micro-nano processing on the front or back of the device to form a periodic columnar structure arranged according to a certain regularity or a hole-like structure to control the incident light [69]. Thus, increases the path of light propagation to increase absorption. Optimizing the geometric parameters of the photon trapping structure can reduce the reflectivity of incident photons. The performance of the device is obviously improved. It is evident that the trapping structure may be good practice in the field of the infrared focal plane array, particularly when it is well-matched with the focal plane array. Currently, this structure has been applied for HgCdTe infrared detectors.

HgCdTe medium-wave infrared (cut-off wavelength 5 μm) detector with different columnar structures and pore structures developed by Raytheon in the United States in 2011 [70]. The results show that the quantum efficiency remains constant in the range of 0.5 and 0.7 for the fill factor, at 4 μm wavelength of light.

In 2013, Pinkie et al. [71] designed a HgCdTe medium-wave infrared detector with a trapping structure. The core idea of this design is to mechanically strip the CdZnTe substrate of HgCdTe. Then directly etch the HgCdTe absorber layer to form the surface microstructure. They used the finite-difference time domain (FDTD) method combined with the finite element method (finite element method) to simulate the structure (simulation software TCAD). Figure 3.18 is a schematic diagram of the designed HgCdTe infrared detector with a height of 5 μm, a bottom diameter of 2 μm, a top diameter of 0.5 μm, and a single-pixel pitch of 8 μm. In Figure 3.18(a), The doping concentration of the narrow bandgap $Hg_{0.715}Cd_{0.285}Te$ layer is n-type lightly

doped $N_D = 1.0 \times 10^{15}$ cm^{-3}, and the doping concentration of the wide bandgap $Hg_{0.60}Cd_{0.40}Te$ layer is p-type lightly doped $N_A = 1.0 \times 10^{17}$ cm^{-3}.

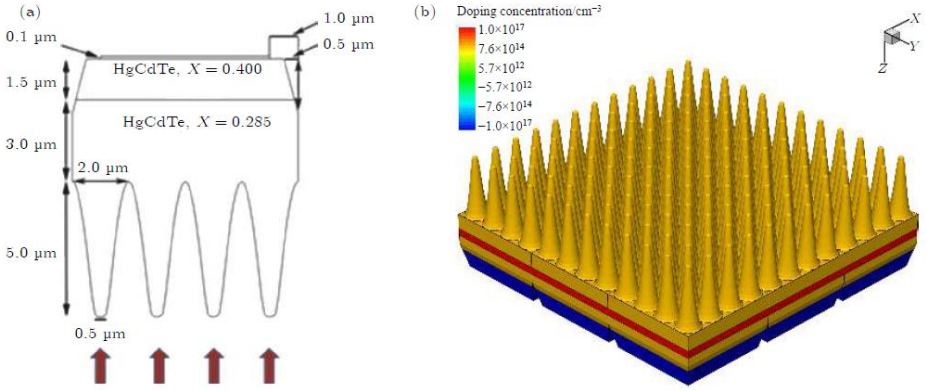

Figure 3.17: Photon trapping structure: (a) Schematic representation of a single-pixel of an array with 8 μm pixels; (b) three-dimensional view of 3 × 3 pixel array (redrawn as in the ref [71]).

The dielectric constant of the HgCdTe infrared detector with a non-trapping structure does not match with the dielectric constant of air, thus a reflection loss occurs about 30% in a device. By properly designing the geometric parameters of the columnar structure, the reflectivity of the device in the range of 1-4.5 μm becomes much less than 1% and as shown in Figure 3.19, the quantum efficiency of the HgCdTe infrared detector with trapping structure is basically maintained at about 90%, which is much larger than the non-trapped structure HgCdTe infrared detector.

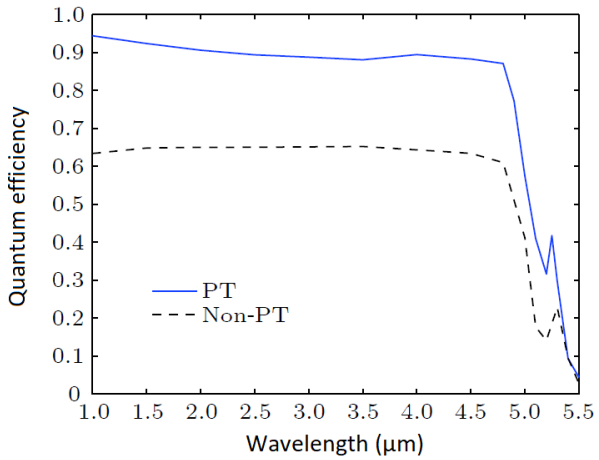

Figure 3.18: Calculated quantum efficiency for the PT and non-PT arrays (redrawn as in the ref [71])

The photon trapping structure will also be applied to the proposed structure to increase quantum efficiency and decrease the dark current. Absorbed power and optical generation rate value need to be calculated to get quantum efficiency of the detector [72]. The absorbed power can be calculated as follows:

$$W = \frac{1}{2}\sigma E^2 \qquad (3.1)$$

Then, the optical carrier generation rate is given by:

$$G_{opt} = \frac{W}{E_{ph}} \qquad (3.2)$$

Detailed simulation results of photon trapping structure is available in the next chapter.

CHAPTER 4

SIMULATION RESULTS AND DISCUSSIONS

It is difficult to predict the impact of the choices made on infrared detectors performance without simulation study. The simulation results become crucial to guide the design of the detectors and the optimal choice of parameters, since the fabrication cycle of the thermal detectors is very long and expensive.

To simulate the proposed structure, COMSOL Multiphysics is used. It offers a seamless interface between electromagnetic and other physics fields, easy identification of mesh parameters and the ability to change management equations. These are the main advantages of COMSOL. In this thesis study, electromagnetics modules of the COMSOL Multiphysics are used to simulate the proposed photodiode.

This chapter is entirely dedicated to the simulation and characterization of the proposed structure. First, the operating principle and layer architecture will be introduced. In the second part of this chapter, simulation parameters are explained. Then, the electrical characterization part is included. The standard p-n photodiode results are also added to this section to see improvements. The last part concerns the presentation of the electro-optical characterization results obtained on the proposed structure.

4.1. The Proposed Structure

The current state of the art HgCdTe infrared photodiodes unfortunately does not allow further exploitation of these structures at high operating temperatures. In order to push back limitations, several HgCdTe-based detection structures have emerged as explained in the previous chapter. A new design was made within the scope of this thesis by making use of previous studies. The proposed design is shown in Figure 4.1. In this structure, a lightly doped absorber layer is added between two highly doped

and high bandgap materials which form the extracting and excluding contacts. Furthermore, a barrier layer has been added to reduce the SRH current. In order to achieve optimal functioning, all device parameters were determined after many simulation studies.

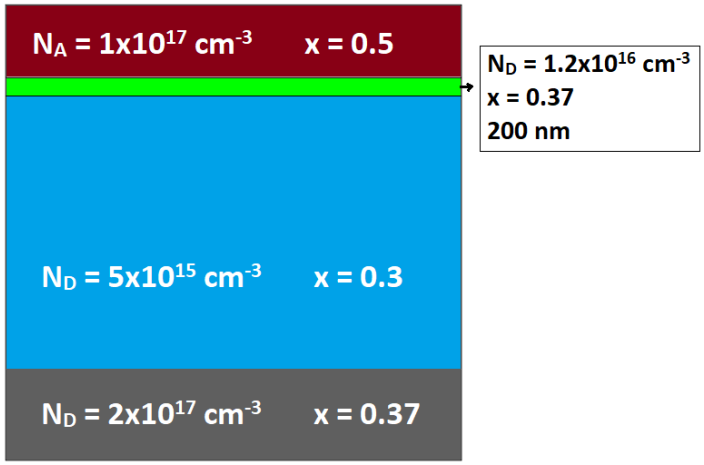

Figure 4.1: Layer architecture of the proposed structure

The different architectures of HgCdTe photodiodes introduced in the previous chapter have the particularity of offering properties that highlight one or the other of the structures according to the applications and the targeted performances. The current characteristics of these photodiode structures show significant differences depending on whether the absorber layer is p-type or n-type.

Barrier thickness and composition have been decided after a parametric sweep study.

Increasing the thickness of the barrier pushes the diffusion behavior toward higher polarizations [8]. Different barrier thicknesses were simulated (Figure 4.2). A thickness of at least 200 nm thus seems necessary.

In the second step we sought to determine the influence of the variation of the composition of the barrier. The evolution of the dark current corresponding to compositions between 0.3 and 0.4 is illustrated in Figure 4.3. The cases 0.30, 0.32 and 0.34 are obviously not viable, leading to a very important SRH current related to the

low barrier height. Cadmium mole fraction of the barrier layer was taken 0.37 to suppress SRH current without degrading quantum efficiency.

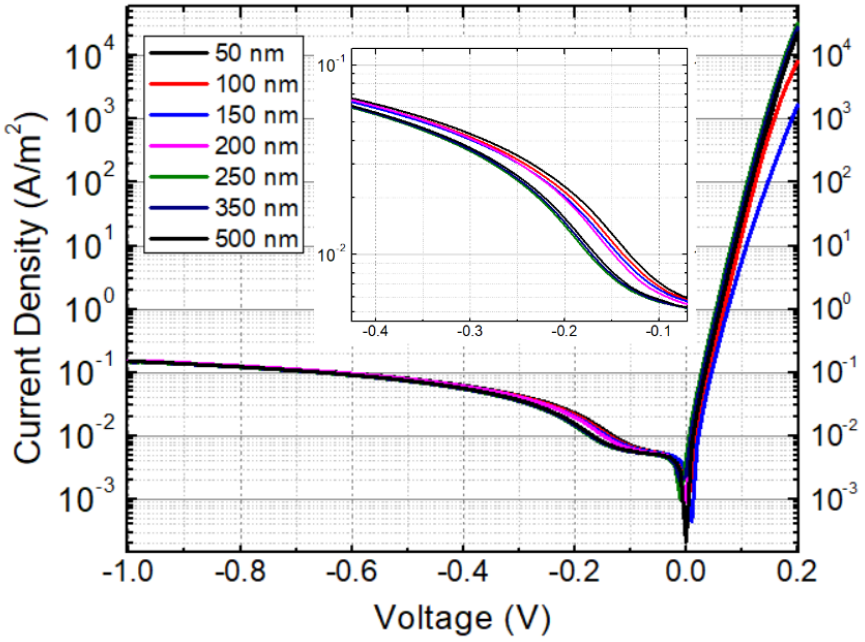

Figure 4.2: Current density vs voltage for various barrier thicknesses (120 K)

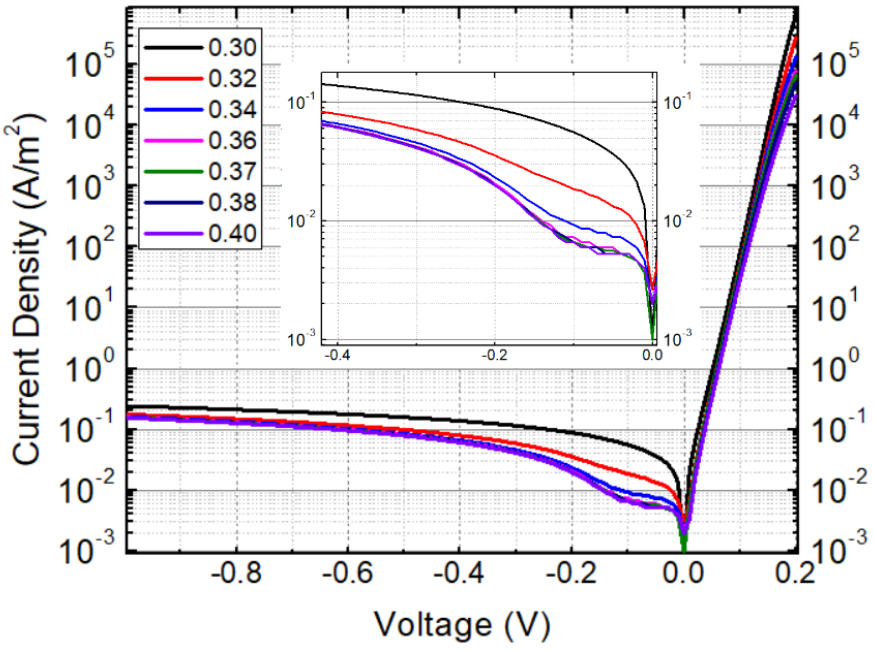

Figure 4.3: Current density vs voltage for various barrier compositions (120 K)

The p-doping is an intrinsic doping obtained by setting the level of mercury vacancies (Hg) in the alloy. This intrinsic doping requires control of temperature and pressure during growth. The level of mercury vacancies in the alloy is fixed by means of an annealing known as "p type annealing" carried out under vacuum at a specific temperature and time. The p-doping is systematically obtained for samples doped intrinsically with the mercury vacancy. On the contrary, an "annealing" is used to lower the rate of these defects, which are preponderant with respect to the other defects present in the crystal lattice. Thus, mercury vacancies create SRH deficiencies that decrease minority carrier lifetime.

Comparing current levels at the same temperature shows that the p on n structures exhibit less dark current than the n on p structures [5]. This is because they offer longer lifetimes as explained above. In summary, the use of n-type doping in the absorber layer generally leads to longer diffusion lengths and allows lower scattering dark currents to be obtained, so the n-type absorber is used in the proposed structure.

Cadmium composition of the layers are $x_{top} = 0.5$, $x_{barrier} = x_{top} = 0.37$, $x_{absorber} = 0.3$ (corresponding to a detection in the MWIR band). The energy band diagram is shown in Figure 4.4.

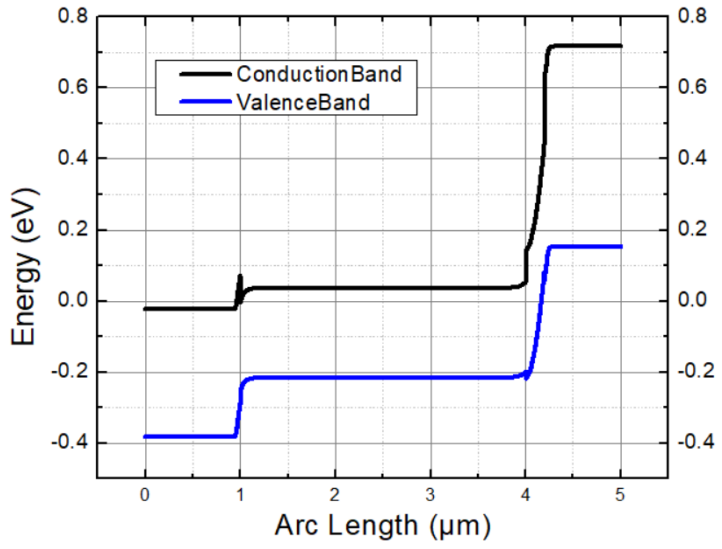

Figure 4.4: Energy band diagram along the device length of the proposed structure

The dark current induced by the diffusion regime is proportional to the doping level, so reducing doping concentration also reduces the diffusion current. However, for very low doping levels (<10^{15} cm^{-3}), the lifetime of the carriers becomes limited by the SRH lifetime and no longer depends on doping. Thus the dark current becomes inversely proportional to the doping and increases with decreasing the doping concentration. There is, therefore, an optimum doping level corresponding to the limit between the SRH regime and the Auger regime which allows the optimization of the dark current. In the proposed structure, the absorber doping level is used as $5x10^{15}$ cm^{-3}.

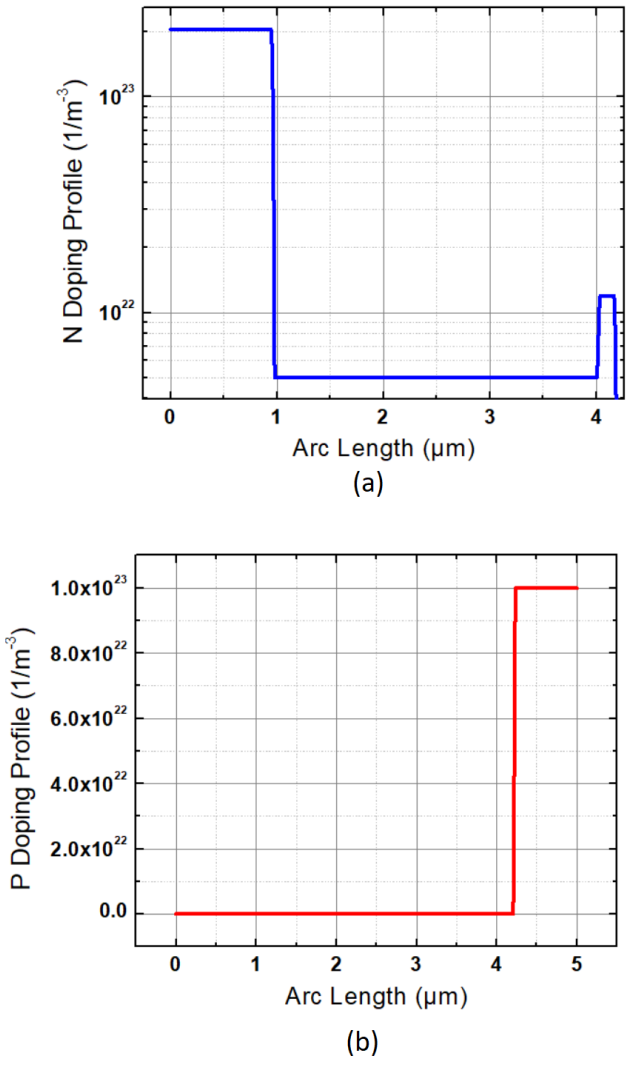

Figure 4.5: (a) N doping profile and (b) P doping profile along the device length

The p-type doping of the HOT device N_A (top) is $1x10^{17}$ cm^{-3} and n-type doping in the bottom layer of the HOT device N_D (bottom) is $2x10^{17}$ cm^{-3} The barrier layer is also n-type doped with the level of $1.2x10^{16}$ cm^{-3} (Figure 4.5).

In the optical side of the study, 25 µm pixel pitch size is used and the photon trapping structure was obtained by dividing one pixel into 6 with a specific aspect ratio (Figure 4.6). The last part of this chapter contains a detailed analysis about the trapping issue.

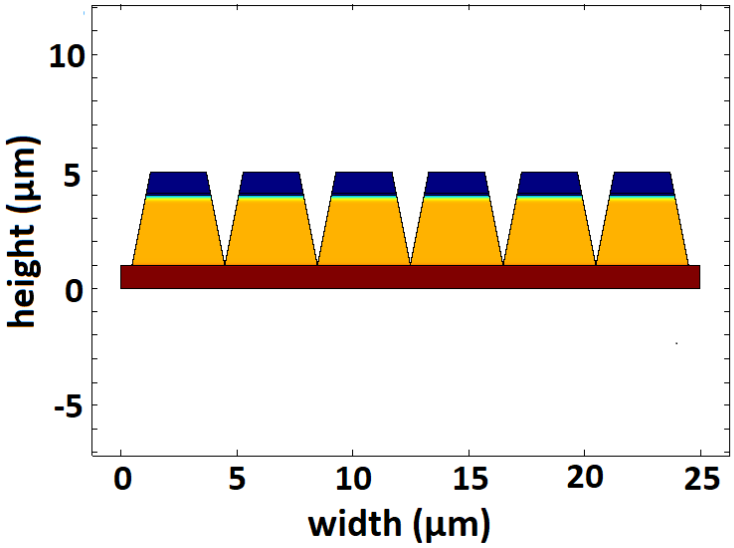

Figure 4.6: Schematic of the proposed photon trapping structure

4.2. Simulation Parameters

Comsol Multiphysics provides you full control over assigning material properties through the Material Browser and Mode Builder. The material library of the Comsol Multiphysics contains more than 2500 materials. These include thermal insulators, minerals, elements, semiconductors, piezoelectric materials and metal alloys.

Unfortunately, this library does not contain HgCdTe. Therefore, the parameters of the material were entered from the literature and it was checked that these parameters were used correctly in equations.

Parameter value can be either a constant or a variable, thus allowing to run sweep parametric studies. This is very convenient to quantify the effect of any material

properties or physical quantities. Within the scope of this thesis, some parameters were used in sweep parametric studies, such as temperature, applied bias, doping level and layer thickness.

The following table details the parameters used to simulate the proposed structure shown in Figure 4.1. For clarity, this table also includes the unit and the description columns.

Table 4.1: The simulation parameters for simulations of the proposed structure [73]

Parameter	Value	Unit	Description
x_{bottom}	0.37	1	Cadmium mole fraction of bottom layer
$x_{absorber}$	0.3	1	Cadmium mole fraction of absorber layer
$x_{barrier}$	0.37	1	Cadmium mole fraction of barrier layer
x_{top}	0.5	1	Cadmium mole fraction of top layer
T	between 100 and 300	K	Temperature
μ_n	$9*b*10^8/(T^{(2a)})$ where a is $(0.2/x)^{0.6}$ and b is $(0.2/x)^{7.5}$	$cm^2/(V*s)$	Electron mobility
μ_h	$\mu_n/100$	$cm^2/(V*s)$	Hole mobility
E_g	$(-0.302+1.93x+(4.31*10^{-4})*T*(1-2x)-0.81x^2+0.832x^3)$	V	Bandgap
X	$4.23-0.813(E_g-0.083)$	V	Affinity
n_i	$(5.24256-3.5729x-4.74019*10^{-4}*T+1.25942*10^{-2}*x*T-5.77046*x^2-4.24123*10^{-6}*T^2)*1e14*E_g^{(0.75)}*T^{(1.5)}*\exp(-E_g*q/(2*k*T))$	$1/cm^3$	Intrinsic carrier concentration
ε	$(20.5-15.6*x+5.7*x^2)$	1	Relative permittivity

$\mathbf{N_{bottom}}$	2×10^{17}	$1/cm^3$	Doping concentration of bottom layer
$\mathbf{N_{absorber}}$	5×10^{15}	$1/cm^3$	Doping concentration of absorber layer
$\mathbf{N_{barrier}}$	1.2×10^{16}	$1/cm^3$	Doping concentration of barrier layer
$\mathbf{N_{top}}$	1×10^{17}	$1/cm^3$	Doping concentration of top layer
k	1.38×10^{-23}	J/K	Boltzmann constant
q	1.602×10^{-19}	C	Electron charge
h	6.62607×10^{-34}	m^2*kg/s	Planck constant
$\mathbf{m_0}$	$9.10938356 \times 10^{-31}$	kg	Electron mass in free space
$\mathbf{m_e}$	$m_0*0.071*E_g$	kg	Effective electron mass
$\mathbf{m_h}$	$0.55*m_0$	kg	Effective hole mass
$\mathbf{N_c}$	$(2*(2*\pi*m_e*(1.38*10^{-23})*T)^{1.5}/((6.62607*10^{-34})^3))$	$1/m^3$	Effective density of states, conduction band
$\mathbf{N_v}$	$(2*(2*\pi*m_h*(1.38*10^{-23})*T)^{1.5}/((6.62607*10^{-34})^3))$	$1/m^3$	Effective density of states, valence band
|F1F2|	0.2	1	Overlap integral
$\boldsymbol{\varepsilon_\infty}$	$15.2-15.6*x+8.2*x^2$	1	High frequency dielectric coefficient
$\mathbf{C_n}$	$((m_e/m_0)*(\|F1F2\|))/(2*(n_i^2)*(3.8*10^{-18})*(\varepsilon_\infty^2)*((1+\mu)^{(0.5)})*(1+2*\mu)) * ((E_g/(k*T))^{(-1.5)})*\exp(-((1+2*\mu)/(1+\mu)) * (E_g/(k*T)))$ Where μ is m_e/m_h	m^6/s	Auger recombination factor, electrons
$\mathbf{C_p}$	$C_n*(1-((3*E_g)/(k*T)))/(1-((5*E_g)/(4*k*T)))$	m^6/s	Auger recombination factor, holes
$\mathbf{G_{rad}}$	$(5.8*10^{-13})*(\varepsilon_\infty^{(0.5)})*((m_0/(m_e+m_h))^{(1.5)}) * (1+(m_0/m_e)+(m_0/m_h))*((300/T)^{(1.5)}) * (E_g^2)+(3*k*T*E_g)+(3.75*(k*T)^2)$	m^3/s	Radiative recombination factor
$\boldsymbol{\tau_{SRH}}$	200	ns	SRH lifetime
Φ	10	W/m^2	Incident Flux Density

Debye length is a critical length parameter for photodiode simulations. It is important to resolve this length scale with the mesh in semiconductor models. It is given by:

$$x = \sqrt{\frac{k_B T \epsilon_0 \epsilon_r}{q^2 N}} \qquad (4.1)$$

where T is the temperature, q is the electron charge, k_B is Boltzmann's constant, ε_r is the relative permittivity of the semiconductor, N is the concentration of ionized acceptors or donors, and ε_0 is the permittivity of free space. This length is about 36 nm for the designed structure at100 K. Therefore, maximum element size in mesh was used less than 36 nm in simulations (between 1 nm and 10 nm).

Another issue is the surface current. Surface recombination velocity in mesa walls was taken as 0 in the trapping structure simulations. If the passivation of mesa walls is not good in the fabricated detector, the surface leakage current may affect the detector performance significantly. This situation should be considered during the fabrication of the designed structure.

4.3. Electrical Characterization of the Proposed Structure

The aim of this study was to compare the performance of the proposed structure in the MWIR range with standard p-n photodiode. This section covers the dark current related simulation results of the proposed structure. The same simulations have been completed for the standard p-n photodiode which is shown in Figure 4.7. Doping levels of absorber layer and p layer are $5x10^{15}$ cm^{-3} and $5x10^{17}$ cm^{-3}, respectively. Cadmium composition and thickness of the absorber layer are the same as the proposed structure.

As mentioned in the previous chapter, the Shockley-Read-Hall recombination mechanism in the depletion zone involves the recombination of the electron-hole pairs via the energy trapping levels (E_t). These trapping levels are located between the conduction band and the valence band and constitute a major source of contribution to the dark current, especially at low temperature. This source of depletion current is,

on the other hand, minimized if the depletion is maintained in the large gap material of the barrier.

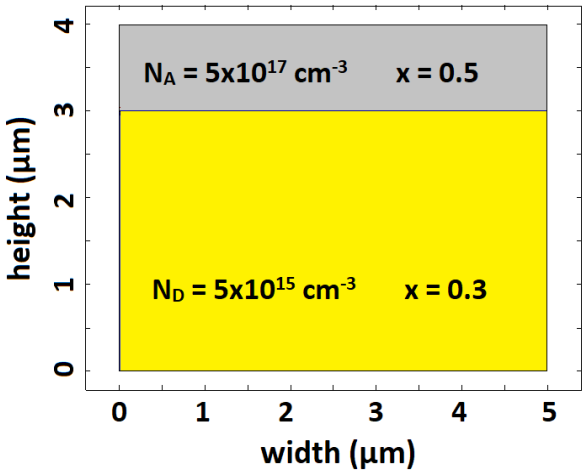

Figure 4.7: Layer architecture of the standard p-n photodiode

In the designed structure, the depletion region is confined completely into the barrier layer (-0.1 V). The electric field is shown in Figure 4.8.

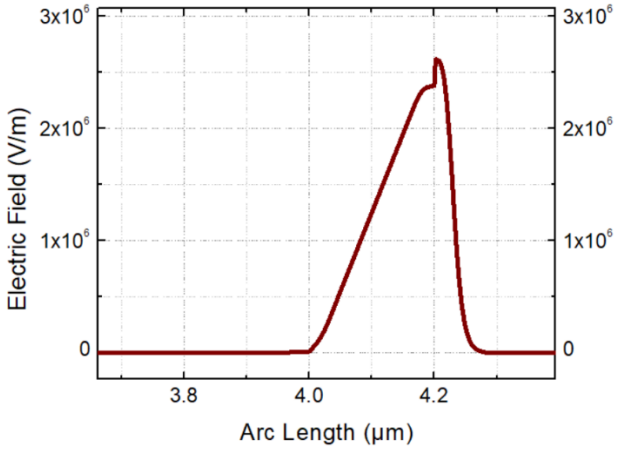

Figure 4.8: Electric field along the device length of the proposed structure

Each dark current component was simulated separately for both structures. The simulation results for 180 K are shown in Figure 4.9. Calculations were performed in steps of 5 mV. SRH lifetime was taken as 200 ns. Auger recombination factor and radiative recombination factor are used as in table 4.1.

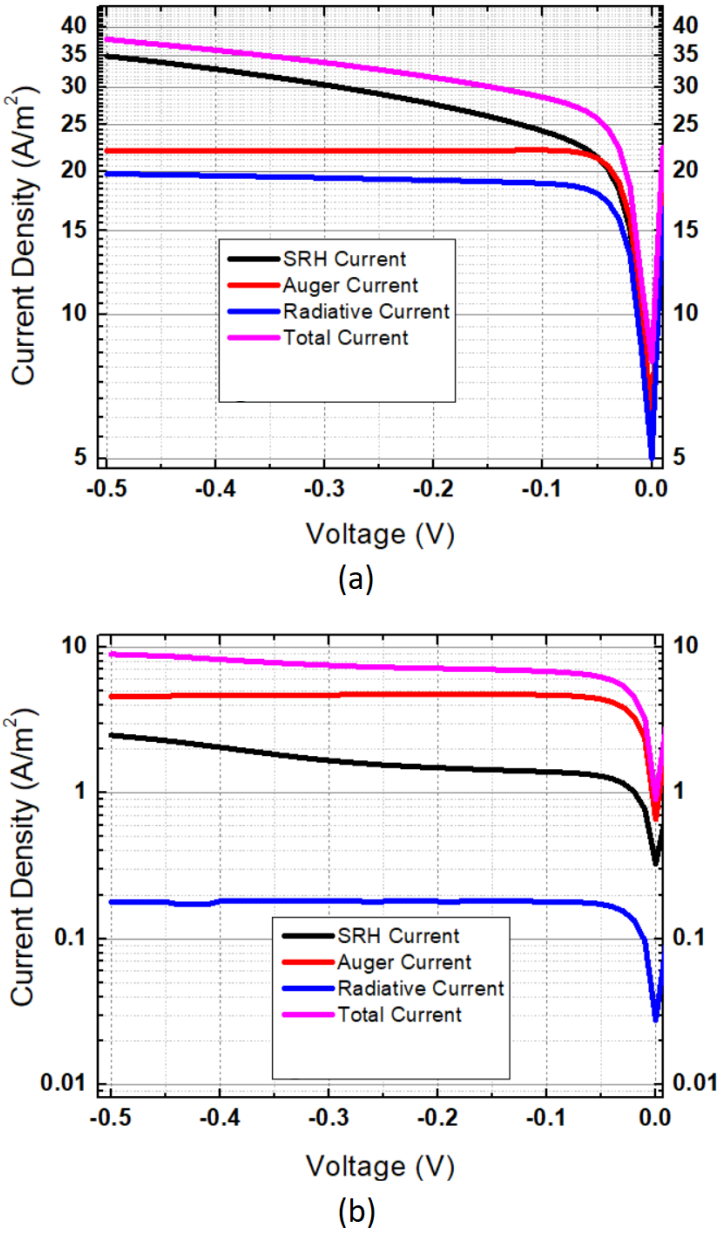

Figure 4.9: Graph of each dark current density component as a function of voltage at a temperature of 180 K for (a) a standard p-n photodiode and (b) the designed structure

Current-voltage simulations were performed at different temperatures, in the range of -0.5 V and 0.3 V (Figure 4.10). SRH lifetime was again taken as 200 ns. Furthermore, the radiative dark current component was also added to simulations, in addition to SRH and Auger. Improvement in the dark current was observed for all temperatures,

especially lower than -0.4 V bias. Thus, simultaneous compression of both dark current components (SRH and Auger) was achieved (Figure 4.10).

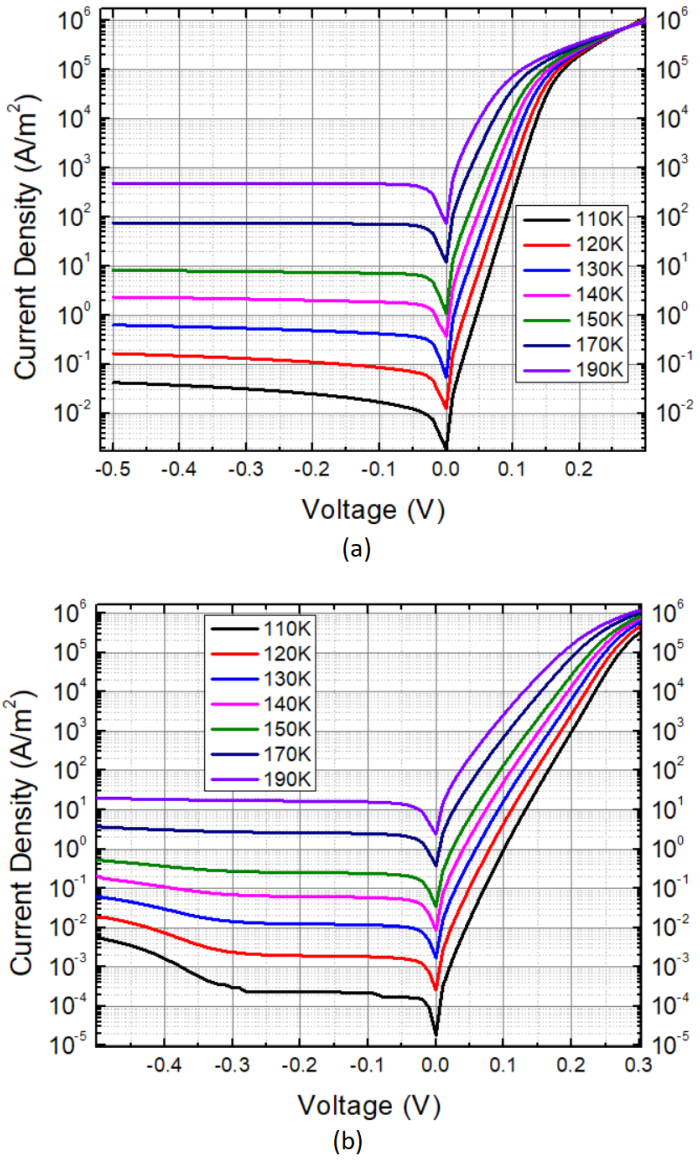

Figure 4.10: Dark current density as a function of voltage for (a) a standard p-n photodiode and (b) the designed structure at temperatures between 110 K and 190 K

As the reverse bias increases, the depletion region expands to the absorber layer and the effectiveness of the barrier starts to decrease. This leads to an increase in dark current at higher reverse biases. Figure 4.11 shows the variation of the depletion region width at different voltage values for 110 K.

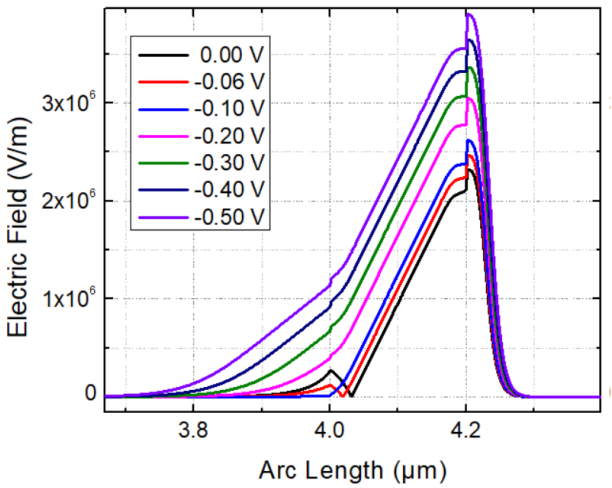

Figure 4.11: E-field along the device length for the designed structure at different reverse biases

The calculated dark current for these two structures shows a significant gain in the dark current over the desired temperature range (Figure 4.12). The current gain in the low temperatures is related to the fact that the proposed structure is limited by Auger recombination whereas the PN photodiode is rather limited under these conditions by the SRH recombinations in the depletion region. On the other hand, the gain at high temperature is due to the Auger Suppression structure which is explained in chapter 3 with details.

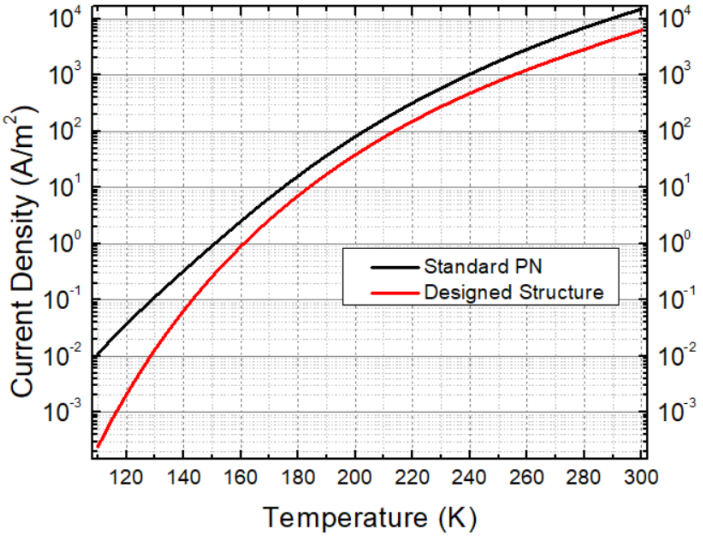

Figure 4.12: Dark current density vs temperature for the designed structure and a standard p-n junction

Photocurrent simulation was also completed with 10 W/m^2 incident flux. The calculated current is shown in Figure 4.13. Valence band discontinuity is 21 meV at -0.1 V in the proposed structure (Figure 4.5). As shown in the figure, there is a reduction in the photocurrent due to this discontinuity, especially at low voltages. Quantum efficiency is also decreased by 3.1% for -0.1 V and 1.1% for -0.2 V. This reduction in performance is eliminated by the trapping structure, which will be explained in the next section.

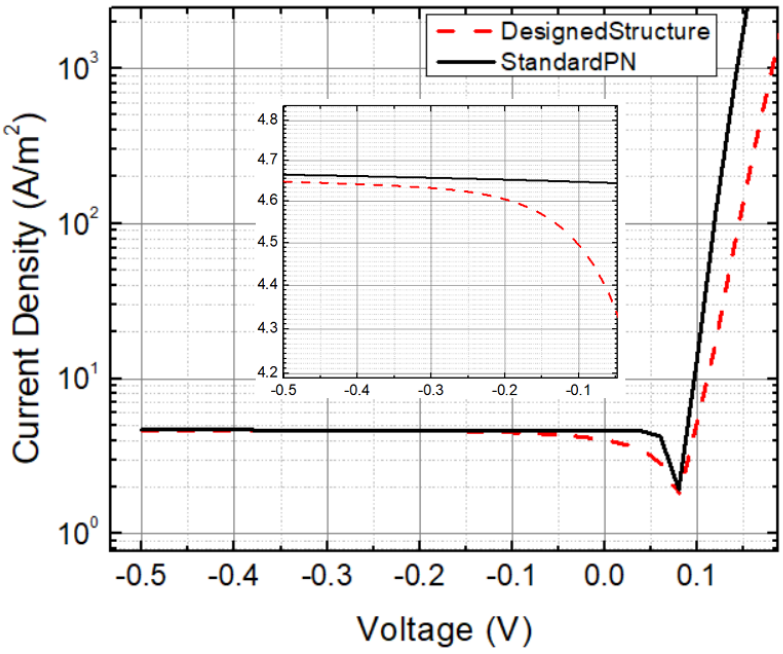

Figure 4.13: Current density as a function of voltage under illumination for the designed structure and a standard p-n junction

4.4. Optical Characterization of the Proposed Structure

In order to obtain the balance between quantum efficiency and detection rate, the thickness of a traditional device is often limited, and the reflection of the incident light will also lead to energy loss. The trapping structure of the traditional infrared detector can reduce reflection and improve the external quantum of the traditional detector. Efficiency, and has a great advantage in improving the integration of focal plane devices. By further controlling the cost and yield of the trapping structure, more applications and developments can be obtained.

Besides, the dark current density is proportional to the volume of the material. Trapping structure can effectively reduce the volume of the device and maintain the total quantum efficiency. Therefore, the performance of the device can be obviously improved.

The proposed trapping structure is shown in Figure 4.6 (similar to Figure 4.14). The aspect ratio of the mesas is 6.66. Widths of the bottom and top of each small mesas are 4 µm and 2.8 µm, respectively. The height of the mesa is 4 µm. Total pitch is 25 µm.

In the scope of this thesis, photo-generated electrical field distribution of the proposed photon trapping structure is calculated with Comsol Multiphysics (Figure 4.14). The device is illuminated from the bottom side. Incident photon flux used 10 W/m^2 at a wavelength of 4 µm.

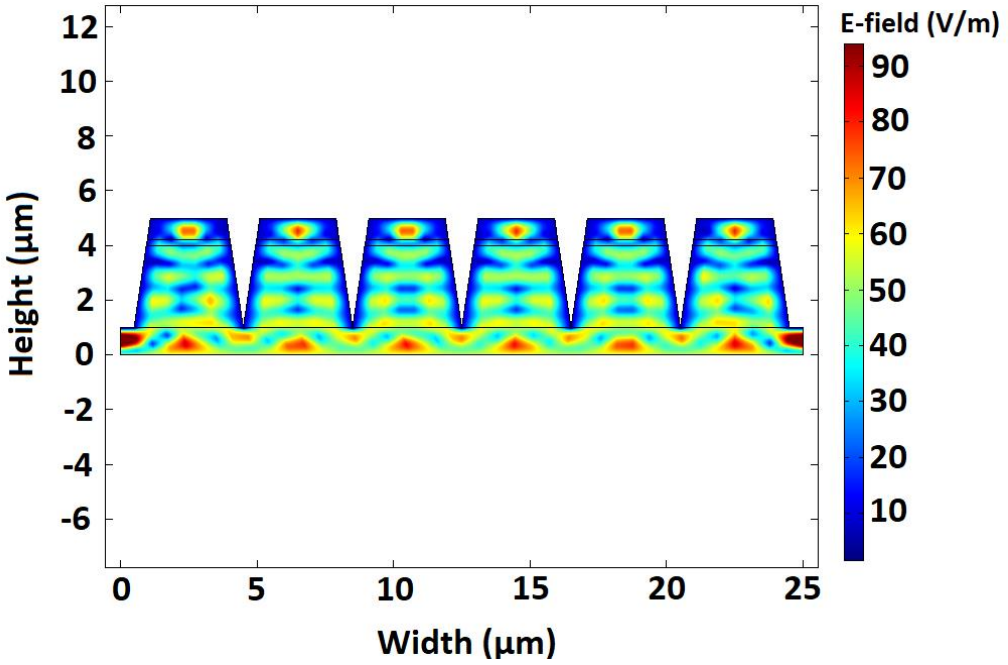

Figure 4.14: Electrical field (V/m) distribution in the photon trapping structure (2D)

From the electrical field distribution, the optical generation rate in the photodiode can be calculated (Equation 3.1 and 3.2). This simulation is done for both standard mesa and photon trapping structure and obtained distributions are shown in Figure 4.15 and

4.16. The calculated total generation in standard mesa structure is 4.18 x 10^{15} (1/m*s). This value is increased to 4.34 x 10^{15} (1/m*s) in the proposed structure.

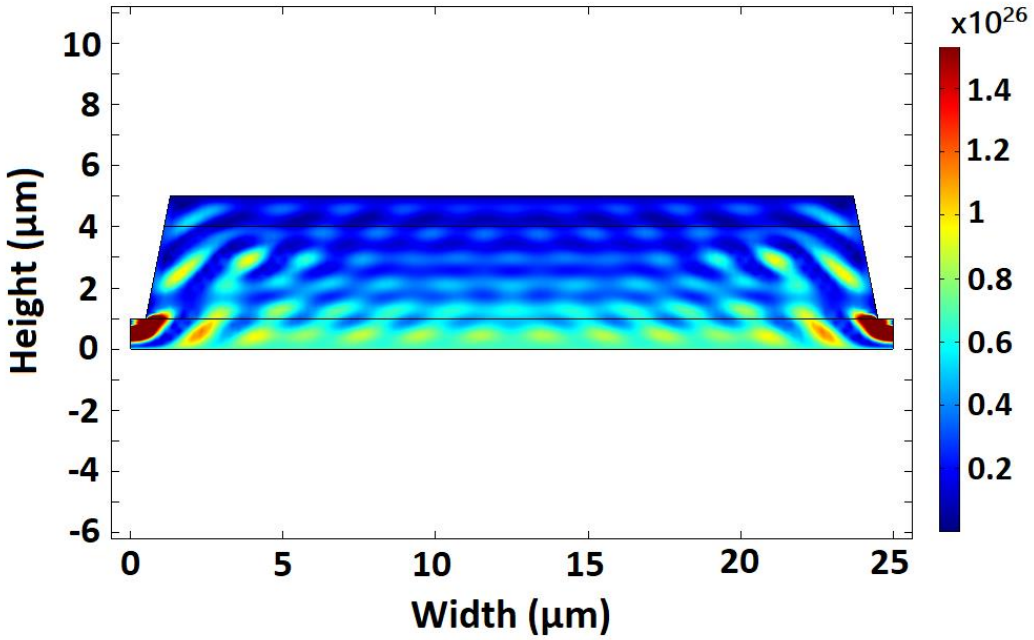

Figure 4.15: Optical generation rate in a standard mesa structure (1/m^3s)

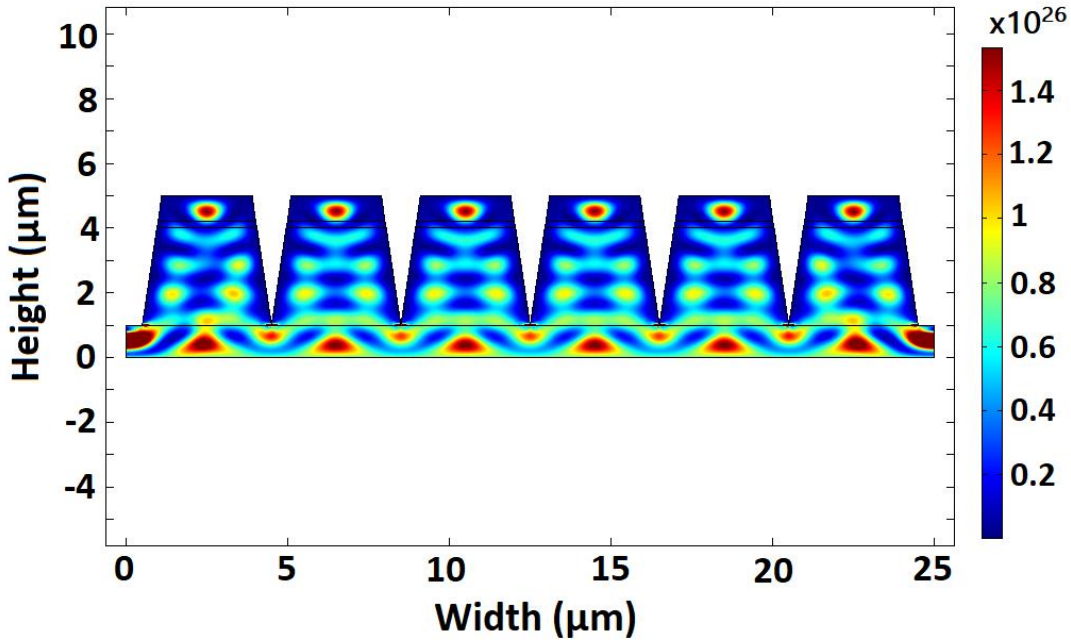

Figure 4.16: Optical generation rate in the proposed trapping structure (1/m^3s)

The dark current at -0.1 V in the photon trapping structure is decreased by 18.2% which corresponds to volume reduction (Figure 4.17).

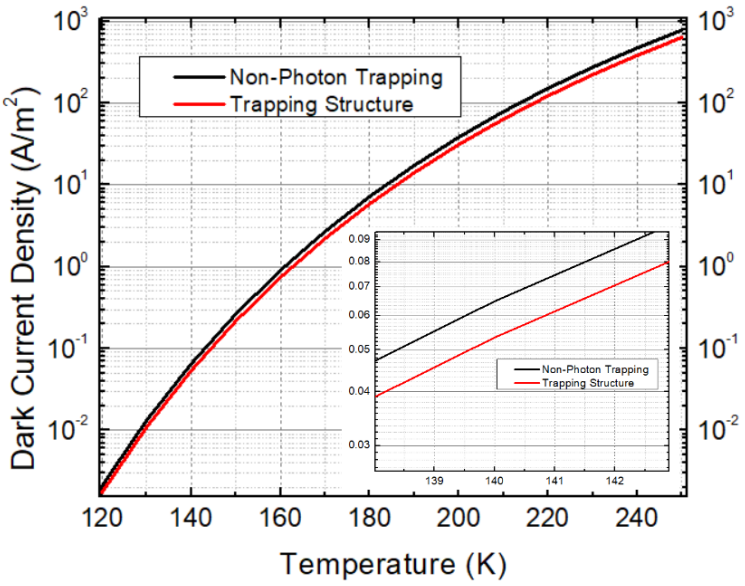

Figure 4.17: Dark current as a function of temperature for trapping and non-trapping structure

Optical generation distributions are used to calculate photocurrent. The photon trapping structure further enhances photon absorption, thereby achieving a 1.9% improvement in photo-current under same illumination (figure 4.18).

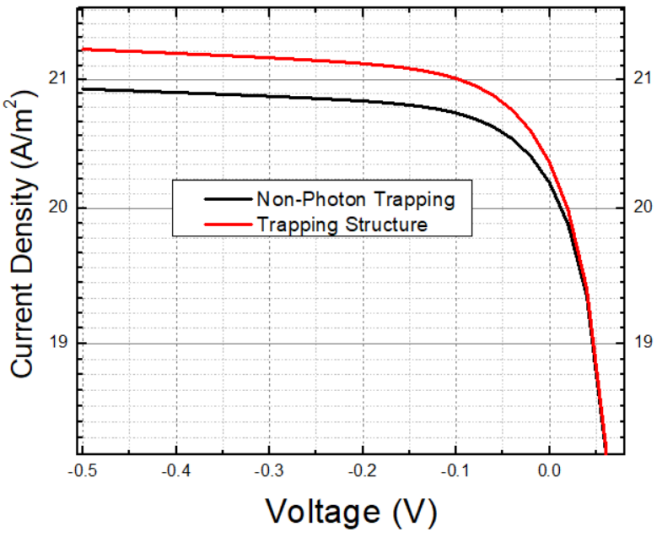

*Figure 4.18: C*urrent as a function of voltage under illumination for trapping and non-trapping

CHAPTER 5

CONCLUSION

Within the scope of this thesis, high operating temperature HgCdTe infrared detectors were studied for MWIR spectral range. Barrier structure, Auger suppression structure and photon trapping structure, which are frequently used in simulation studies in the literature, are simulated separately by COMSOL Multiphysics and their results are compared with the standard p-n photodiode. In addition, a new structure was designed which can reduce dark current at all temperatures.

The auger suppression structure is also called non-equilbrium operation and provides a significant reduction in dark current at high operating temperatures. This structure is formed by the fact that the lightly doped absorber is located between two layers of high doped and high bandgap. In the case of high inverse bias, the carrier density in the absorber decreases and therefore Auger processes drops. In both reference studies and simulations, it has been shown that the reduction in the dark current is around 12 times at temperatures above 200 K.

High SRH current may occur due to impurities or dislocations, especially at low temperatures. This is generally the case when using alternative substrates (Si, GaAs) during crystal growth. The barrier structure is used to reduce the SRH current in such cases. This structure is achieved by adding a high bandgap layer to the center of the standard p-n photodiode structure. The reduction (~50 times below 120 K) in the dark current at low temperatures was shown by simulations. However, quantum efficiency also decreased by 3.1%.

The photon trapping structure is another high operating temperature (HOT) structure. In this structure, it is aimed to prevent the decrease in absorption due to reflections. By changing the shapes of each pixel, high absorption can be achieved with a reduced volume of material. In order to reduce reflection, the mesa structure was manipulated

and the change in the optical generation rate was simulated in the proposed structure. In addition, improvement in the dark current was observed due to the reduced volume of the material.

By examining the above mentioned HOT structures, a new structure is proposed and the simulations of this structure were completed with Comsol Multiphysics. The Auger, Shockley Read Hall (SRH) and radiative components of the dark current were simulated separately and compared with the standard p-n photodiode. The dark current is also calculated for different temperatures. With the designed structure, it was observed that the dark current improved at all temperatures between 100 K and 300 K. In quantum efficiency, 3.1% reduction was observed for the -0.1 V (reverse bias) due to barrier layer (valence band discontinuity). However, this reduction was reduced to 1.2% by photon trapping structure. The photon trapping structure also provided an improvement of about 18.2% in the dark current.

REFERENCES

[1] H. Kocer, Ph.D. thesis, METU, 2011.

[2] C. Beşikçi, “Infrared Devices and Systems Lecture Notes”, no. September, pp. 1-245, 2015.

[3] PL Richards, “Bolometers for infrared and millimeter waves”, Journal of Applied Physics, pp. 76-124, 1994.

[4] D. J. Smith, T. Aoki, J. K. Furdyna, X. Liu, M. R. McCartney, and Y. H. Zhang, “Atomic-scale characterization of (mostly zincblende) compound semiconductor heterostructures,” J. Phys. Conf. Ser., vol. 471, no. 1, 2013.

[5] P. Y. Emelie, Ph.D. thesis, The University of Michigan, 2009.

[6] C. H. Lin and C. W. Liu, “Metal-insulator-semiconductor photodetectors,” Sensors, vol. 10, no. 10, pp. 8797–8826, 2010.

[7] D. Vasileska, S. M. Goodnick, and G. Klimeck, Computational electronics: Semiclassical and quantum device modeling and simulation. 2017.

[8] Anne M. Itsuno, Ph.D. thesis, The University of Michigan, 2014.

[9] G. Remarks, “DandM Figures,” pp. 1–10.

[10] M. Planck and A. Einstein, “1 Basics of Optical Emission and Absorption.”

[11] L. Lei et al., “Long-wavelength interband cascade infrared photodetectors towards high temperature operation,” Quantum Sens. Nano Electron. Photonics XIV, vol. 10111, no. January 2017, p. 1011113, 2017.

[12] L. Pillans, R. M. Ash, L. Hipwood, and P. Knowles, “MWIR mercury cadmium telluride detectors for high operating temperatures,” Infrared Technol. Appl. XXXVIII, vol. 8353, no. May 2012, p. 83532W–83532W–12, 2012.

[13] N. K., R. Dat, and A. K., “phase diagram for the pseudo-binary CdTe-HgTe - Advances in Infrared Detector Array Technology,” Optoelectron. - Adv. Mater. Devices, 2013.

[14] S. Eminoglu et al., “A 640×512-20μm dual-polarity ROIC for MWIR and LWIR hybrid FPAs,” Infrared Technol. Appl. XLII, vol. 9819, no. June 2016, p. 981928, 2016.

[15] A. Sosna et al., “Higher operation temperature quadrant photon detectors of 2-11 μm wavelength radiation with large photosensitive areas,” vol. 1043505, no. October 2017, p. 6, 2017.

[16] P. Norton, “HgCdTe infrared detectors,” Opto-electronics Rev., vol. 10, no. 3, pp. 159–174, 2002.

[17] B. D. MacLeod and D. S. Hobbs, “Long life, high performance anti-reflection treatment for HgCdTe infrared focal plane arrays,” Infrared Technol. Appl. XXXIV, vol. 6940, no. April 2008, p. 69400Y, 2008.

[18] A. Rogalski, “HgCdTe infrared detector material: History, status and outlook,” Reports Prog. Phys., vol. 68, no. 10, pp. 2267–2336, 2005.

[19] A. Manissadjian, P. Costa, P. M. Tribolet, and G. L. Destefanis, “HgCdTe performance for high operating temperatures,” Infrared Technol. Appl. XXIV, vol. 3436, no. October 1998, p. 150, 2004.

[20] W.D. Lawson, S. Nielsen, E.H. Putley, and A.S. Young, “Prepa- ration and Properties of HgTe and Mixed Crystals of HgTe-CdTe,”J. Phys. Chem. Solids 9, 325–329, 1959.

[21] G.L. Hansen, J.L. Schmidt, T.N. Casselman,, “Energy gap versus alloy composition and temperature in Hg1-xCdxTe” J. Appl. Phys. 53, 7099–7101, 1982.

[22] P. Capper, “Properties of narrow gap cadmium-based compounds”, pages 80-85, 1994.

[23] W. E. Tennant, J. M. Arias, and J. Bajaj, “HgCdTe at Teledyne,” no. May 2009, p. 72982V, 2009.

[24] D. A. Ramirez, E. A. Plis, S. A. Myers, C. P. Morath, V. M. Cowan, and S. Krishna, “High-operating temperature MWIR unipolar barrier photodetectors based on strained layer superlattices,” Infrared Technol. Appl. XLI, vol. 9451, no. June 2015, p. 945113, 2015.

[25] H. F. Schaake et al., “High-operating-temperature MWIR detector diodes,” J. Electron. Mater., vol. 37, no. 9, pp. 1401–1405, 2008.

[26] H. Figgemeier et al., “State of the art of AIM LWIR and VLWIR MCT 2D focal plane detector arrays for higher operating temperatures,” Infrared Technol. Appl. XLII, vol. 9819, no. May 2016, p. 98191C, 2016.

[27] H. Figgemeier et al., “State-of-the-art MCT photodiodes for cutting-edge sensor applications by AIM,” Infrared Technol. Appl. XLIII, vol. 10177, no. May 2017, p. 101771K, 2017.

[28] J. Jenkins et al., “Fabrication of small pitch, high definition (HD) 1kx2k/5µm MWIR focal-plane-arrays operating at high temperature (HOT),” Infrared Technol. Appl. XLIII, vol. 10177, no. May 2017, p. 101771J, 2017.

[29] G. D. Skidmore, “Uncooled 10µm FPA development at DRS,” Infrared Technol. Appl. XLII, vol. 9819, no. May 2016, p. 98191O, 2016.

[30] C. Besikci, “Extended short wavelength infrared FPA technology: status and trends,” no. January, p. 23, 2018.

[31] J. G. Pellegrino, R. DeWames, P. Perconti, C. Billman, and P. Maloney, “HOT MWIR HgCdTe performance on CZT and alternative substrates,” Infrared Technol. Appl. XXXVIII, vol. 8353, no. May 2012, p. 83532X–83532X–7, 2012.

[32] S. Velicu et al., “Two color high operating temperature HgCdTe photodetectors grown by molecular beam epitaxy on silicon substrates,” Nanophotonics Macrophotonics Sp. Environ. VII, vol. 8876, no. September 2013, p. 887608, 2013.

[33] N. H. Jo et al., “Two-dimensional numerical simulation of HgCdTe infrared detectors,” Infrared Technol. Appl. XXIV, vol. 3436, no. July, p. 50, 2004.

[34] T. K. Parashar, “Theoretical Modelling of Basics Parameters of HgCdTe Material,” vol. 6, no. 11, pp. 295–303, 2017.

[35] W. van Roosbroeck, and W. Shockley, “Photon-Radiative Recombination of Electrons and Holes in Germanium” Phys. Rev. 94-1558, 1954.

[36] R. N. Hall, Proc. Inst. Electr. Eng. Part B, Suppl. 106-923, 1959.

[37] P. E. Petersen, “Auger Recombination in Hg1−xCdxTe”, Journal of Applied Physics, 41, 3465 (1970).

[38] A. D. D. Dwivedi and P. Chakrabarti, “Analytical Modeling and Numerical Simulation of Hg1-xCdxTe Based N+n0p+ Photodetector for MWIR Free Space Optical Communication,” Int. J. Adv. Appl. Phys. Res., vol. 2, no. 2, pp. 20–27, 2015.

[39] C. H. Grein, M. E. Flatté, and Y. Chang, “Modeling of recombination in HgCdTe,” J. Electron. Mater., vol. 37, no. 9, pp. 1415–1419, 2008.

[40] M.A. Kinch, M. J. Brau, and A. Simmons, J. Appl. Phys. 44, 1649 (1973).

[41] W. Shockley, and W.T. Hall, Physical Review. 87, 835 (1952).

[42] R.N. Hall, Physical Review. 87, 387 (1952).

[43] Patrik Scajev, Ph.D. thesis, Vilnius University, 2013.

[44] D. Vasileska, “Drift-Diffusion Model: Time-Dependent Simulations Sharfetter-Gummel Discretization,” p. 11.

[45] C. Bonfil, “The Drift Diffusion Simulation of Coupled Ionic-Electronic Devices,” pp. 24–27, 2014.

[46] N. D. Akhavan, G. Jolley, G. A. Umana-Membreno, J. Antoszewski, and L. Faraone, “Performance modeling of bandgap engineered HgCdTe-based nBn infrared detectors,” IEEE Trans. Electron Devices, vol. 61, no. 11, pp. 3691–3698, 2014.

[47] N. D. Akhavan, G. Jolley, G. A. Umana-Membreno, J. Antoszewski, and L. Faraone, “Theoretical Study of Midwave Infrared HgCdTe nBn Detectors Operating at Elevated Temperatures,” J. Electron. Mater., vol. 44, no. 9, pp. 3044–3055, 2015.

[48] P. Martyniuk*, M. Kopytko, and A. Rogalski, “Barrier infrared detectors P.” Opto−Electron. Rev., 22, no. 2, 2014.

[49] M. Kopytko et al., “ MOCVD grown HgCdTe p + BnN + barrier detector for MWIR HOT operation ,” Infrared Technol. Appl. XLI, vol. 9451, no. June 2015, p. 945117, 2015.

[50] E. Plis, S. A. Myers, D. A. Ramirez, and S. Krishna, “Development of dual-band barrier detectors,” Infrared Technol. Appl. XLII, vol. 9819, no. May 2016, p. 981911, 2016.

[51] M. Kopytko and P. Martyniuk, “HgCdTe Mid- and Long-Wave Barrier Infrared Detectors for Higher Op200erating Temperature Condition,” Model. Simul. Eng. Sci., no. September, pp. 70–90, 2016.

[52] P. Martyniuk, “HOT HgCdTe infrared detectors,” Proc. Int. Conf. Numer. Simul. Optoelectron. Devices, NUSOD, pp. 173–174, 2014.

[53] Y. Ozer and S. Kocaman, “A comparative design study for MWIR HgCdTe detectors,” Infrared Technol. Appl. XLIII, vol. 10177, no. May 2017, p. 101771H, 2017.

[54] Y. Ozer and S. Kocaman, “Generation recombination suppression via depletion engineered heterojunction for alternative substrate MWIR HgCdTe infrared photodetectors,” J. Appl. Phys., vol. 122, no. 14, 2017.

[55] R. Gu, W. Lei, J. Antoszewski, I. Madni, G. Umana-Menbreno, and L. Faraone, “Recent progress in MBE grown HgCdTe materials and devices at UWA,” Infrared Technol. Appl. XLII, vol. 9819, no. May 2016, p. 98191Z, 2016.

[56] P. Martyniuk, W. Gawron, and A. Rogalski, “Theoretical modeling of HOT HgCdTe barrier detectors for the mid-wave infrared range,” J. Electron. Mater., vol. 42, no. 11, pp. 3309–3319, 2013.

[57] S. Myers et al., “Photoconductive gain in barrier heterostructure infrared detectors,” no. May 2012, p. 83532Z–83532Z–10, 2012.

[58] A. Kębłowski et al., “Progress in MOCVD growth of HgCdTe epilayers for HOT infrared detectors,” Infrared Technol. Appl. XLII, vol. 9819, no. May 2016, p. 98191E, 2016.

[59] T. Ashley and C. T. Elliot, “Non-equilibrium devices for infrared detection,” Electron. Lett, vol. 21, no. 10, pp. 451-452, 1985.

[60] J. Schuster, W. E. Tennant, E. Bellotti, and P. S. Wijewarnasuriya, “Analysis of the auger recombination rate in P + N−n−N−N HgCdTe detectors for HOT applications,” no. June 2016, p. 98191F, 2016.

[61] M. Nadimi and A. Sadr, “Modeling and Simulation of High Operating Temperature MWIR Photo Detector Based on Mercury Cadmium Telluride,” Int. J. Comput. Electr. Eng., vol. 3, no. 4, pp. 597–599, 2012.

[62] W. Gawron, A. Rogalski, J. Piotrowski, P. Martyniuk, and P. Madejczyk, “Modeling of HgCdTe LWIR detector for high operation temperature conditions,” Metrol. Meas. Syst., vol. 20, no. 2, pp. 159–170, 2013.

[63] W. Taylor, P. S. Wijewarnasuriya, Y. Chen, G. Brill, and N. K. Dhar, “Mercury Cadmium Telluride for High Operating Temperature Infrared Detectors,” no. 211, pp. 0–8.

[64] S. Velicu, C. H. Grein, P. Y. Emelie, A. Itsuno, J. D. Phillips, and P. Wijewarnasuriya, “Non-cryogenic operation of HgCdTe infrared detectors,” Quantum Sens. Nanophotonic Devices VII, vol. 7608, no. January 2010, p. 760820, 2010.

[65] J. Liang et al., “Improved performance of HgCdTe infrared detector focal plane arrays by modulating light field based on photonic crystal structure,” J. Appl. Phys., vol. 115, no. 18, 2014.

[66] K. D. Smith et al., “High operating temperature mid-wavelength infrared HgCdTe photon trapping focal plane arrays,” Infrared Technol. Appl. XXXVIII, vol. 8353, no. May 2012, p. 83532R–83532R–7, 2012.

[67] H. Sharifi et al., “Fabrication of high-operating temperature (HOT), visible to MWIR, nCBn photon-trap detector arrays,” Infrared Technol. Appl. XXXIX, vol. 8704, no. June 2013, p. 87041U, 2013.

[68] J. Schuster, B. Pinkie, S. Tobin, C. Keasler, D. D’Orsogna, and E. Bellotti, “Numerical simulation of third-generation HgCdTe detector pixel arrays,” IEEE J. Sel. Top. Quantum Electron, vol. 19, no. 5, 2013.

[69] P. Zhang, Z. H. Ye, C. Lin, X. N. Hu, R. J. Ding, and L. He, “Structure design of HgCdTe mid-wavelength photon trapping infrared focal plane arrays,” 13th Int. Conf. Numer. Simul. Optoelectron. Devices, NUSOD 2013, pp. 129–130, 2013.

[70] J. G. A. Wehner, E. P. G. Smith, G. M. Venzor, K. D. Smith, A. M. Ramirez, B. P. Kolasa, K. R. Olsson, and M. F. Vilela, “HgCdTe photon trapping structure for broadband mid-wavelength infrared absorption,” J. Electron. Mater. 40, 1840 (2011).

[71] Benjamin Pinkie, Jonathan Schuster, and Enrico Bellotti, “Physics-based simulation of the modulation transfer function in HgCdTe infrared detector arrays”, Vol. 21, Issue 12, pp. 14712-14727, 2013.

[72] M. Vallone et al., “Broadband 3D optical modeling of HgCdTe infrared focal plane arrays,” Proc. Int. Conf. Numer. Simul. Optoelectron. Devices, NUSOD, pp. 205–206, 2017.

[73] S. Bae, H. Jung, S. H. Kim, N. H. Kim, S.-M. Park, and H. C. Lee, “HgCdTe technologies in South Korea,” Infrared Technol. Appl. XXXV, vol. 7298, no. May 2009, p. 72982Y, 2009.